nature neuroscience

Parallel processing by cortical inhibition enables context-dependent behavior

Kishore V Kuchibhotla[1,2], Jonathan V Gill[1,2], Grace W Lindsay[3], Eleni S Papadoyannis[1,2], Rachel E Field[1,2], Tom A Hindmarsh Sten[1,2], Kenneth D Miller[3] & Robert C Froemke[1,2]

© 2017 Nature America, Inc., part of Springer Nature. All rights reserved.

Physical features of sensory stimuli are fixed, but sensory perception is context dependent. The precise mechanisms that govern contextual modulation remain unknown. Here, we trained mice to switch between two contexts: passively listening to pure tones and performing a recognition task for the same stimuli. Two-photon imaging showed that many excitatory neurons in auditory cortex were suppressed during behavior, while some cells became more active. Whole-cell recordings showed that excitatory inputs were affected only modestly by context, but inhibition was more sensitive, with PV$^+$, SOM$^+$, and VIP$^+$ interneurons balancing inhibition and disinhibition within the network. Cholinergic modulation was involved in context switching, with cholinergic axons increasing activity during behavior and directly depolarizing inhibitory cells. Network modeling captured these findings, but only when modulation coincidently drove all three interneuron subtypes, ruling out either inhibition or disinhibition alone as sole mechanism for active engagement. Parallel processing of cholinergic modulation by cortical interneurons therefore enables context-dependent behavior.

Sensory stimuli convey critical information about various types of opportunities and threats, including access to nourishment, the presence of predators, and the needs of infants. The same sensory stimulus, however, can have different meanings depending on previous learned associations and the contexts within which it is presented[1–9]. For example, in language processing, the same words often have multiple meanings. Humans determine the meaning of these words by integrating prior knowledge with context to converge on a relevant interpretation[10,11]. How does the brain enable such interpretation of sensory cues based on behavioral context? We propose that three network features would enable context-dependent processing of external stimuli by neural circuits: some components must be stable and provide a high-fidelity representation of a sensory stimulus independent of context; other components must be dynamic and rapidly adjust when context changes; and, finally, there must be instructive signals that convey the global contextual milieu.

The mammalian auditory cortex is a major site of contextual modulation during acoustic behaviors, such that task engagement alters the spiking of principal neurons even when there is no change in the external sensory cue[1–4,12–18]. Whether or not a stimulus will produce one or more action potentials depends on the strength and timing of excitatory and inhibitory synaptic inputs. In the adult, excitatory and inhibitory inputs are correlated during passive presentation of acoustic stimuli; this co-tuning and correlation of synaptic responses is referred to as 'excitatory–inhibitory balance'[19–24]. However, episodes of learning and periods of heightened attention or arousal activate neuromodulatory systems that can lead to the transient uncoupling of excitation from inhibition. This temporary period of increased excitability is effective at inducing long-term modifications of synaptic strength and receptive field organization[25–27]. For example, pairing stimulation of the cholinergic nucleus basalis with presentation of an acoustic stimulus leads to long-term changes in the receptive field properties of auditory cortical neurons[28,29], via changes in inhibition[25]. Cholinergic activity also contributes to task performance by signaling positive and negative reinforcement, potentially through cortical interneurons[6,30–32]. These links between neuromodulation, inhibitory synaptic transmission, and behavioral changes may be a general feature of nervous system organization. For example, a recent study showed that cholinergic activation of dendritic inhibition in the hippocampus can enable fear learning[33].

Context-dependent activity, however, requires rapid changes on a trial-to-trial basis. Neuronal ensembles must adjust their firing rate in a reversible manner based solely on contextual cues[2,4,13,15]. These types of context-dependent responses diverge from the longer-term memory traces and reinforcement mechanisms that have been previously described[6,25,30,33] but may co-opt some of the underlying circuitry. The relationship between excitation and inhibition may simply scale (up or down) based on attentional demands. However, such co-tuned scaling might restrict state-dependent flexibility. Instead, theoretical work suggests that inhibitory inputs can be preferentially regulated by neuromodulation[34]. These synaptic and circuit mechanisms have been difficult to resolve because of the need to monitor complex input–output dynamics of excitatory, inhibitory and neuromodulatory inputs. Here we take an integrative approach to measure, manipulate, and model

[1]Skirball Institute, Neuroscience Institute, Departments of Otolaryngology, Neuroscience and Physiology, New York University School of Medicine, New York, New York, USA. [2]Center for Neural Science, New York University, New York, New York, USA. [3]Center for Theoretical Neuroscience, Department of Neuroscience, Swartz Program in Theoretical Neuroscience, Kavli Institute for Brain Science, Columbia University, New York, New York, USA. Correspondence should be addressed to R.C.F. (robert.froemke@med.nyu.edu).

Received 8 August; accepted 1 October; published online 31 October 2016; doi:10.1038/nn.4436

the impact of behavioral engagement on a cortical circuit in behaving mice. We combine (i) cell-type-specific two-photon calcium imaging to measure network output, (ii) whole-cell voltage-clamp recordings of excitatory and inhibitory inputs, (iii) calcium imaging of cholinergic axons to monitor neuromodulatory inputs, (iv) optogenetics to manipulate all core components of the circuit, and (v) a theoretical model to integrate and test the robustness of our findings.

RESULTS

A context-switching task that depends on the auditory cortex

To determine how behavioral context influence network dynamics, we trained head-fixed mice on an active versus passive context-switching task using a block-based experimental design (**Fig. 1a**, **Supplementary Fig. 1a**). For the active listening context ('active context'), we trained animals on an auditory go/no-go stimulus recognition task. Mice learned to lick for a water reward provided through a lick tube after hearing the reinforced conditioned stimulus (the target tone, **Supplementary Fig. 1b**) and to refrain from licking after hearing an unrewarded pure tone of a different frequency (the foil tone, **Supplementary Fig. 1c**). In the passive context, the lick tube was removed and mice were exposed to the same sounds (target and foil), but they did not produce a behavioral response (**Supplementary Video 1**). Importantly, the absence of licking in the passive context (i.e., the sensorimotor response in response to the target tone) was completely voluntary since it was not reinforced with reward or punishment. The choice to behave was therefore externally triggered by the presence or absence of the lick tube. This task required auditory cortex, as bilateral muscimol infusions into auditory cortex significantly impaired behavioral performance in the active context (**Fig. 1b**; $n = 3$ animals, $d' = 3.0 \pm 0.2$, muscimol $d' = 0.8 \pm 0.3\%$, mean ± s.e.m. (where d' is the difference between z-scored hit rate and false alarm rate); $P < 0.05$, Student's paired two-tailed t-test).

Rapid and reversible context-dependent changes in A1 network output

To determine how auditory cortex responds to the conditioned stimuli in both contexts, we first imaged the activity of 1,595 neurons in cortical layer 2/3 in five mice in the two different contexts. To select the target and foil tones, we performed two-photon imaging in awake mice virally transduced to express the calcium indicator GCaMP6s while presenting pure tones between 4 and 64 kHz at a sound pressure level (SPL) of 70 dB before behavioral training (**Fig. 1c**,**d**). We used two criteria in selecting the stimuli: (1) the imaged focal planes had neurons with tone-evoked calcium responses to the target and foil (**Fig. 1c**) and (2) the two tones were within one octave of each other (**Fig. 1d**). After selecting the target and foil, we conducted behavioral training (**Fig. 1e** and **Supplementary Fig. 1d**) until mice reliably responded to the target tone with licking (hits) and withheld licking responses to the foil tone (correct rejects) (**Fig. 1e**, $n = 23$ mice, $d' = 2.5 \pm 0.3$, hit rate = 92.5 ± 1.7%, mean ± s.e.m.). All mice reached threshold within 3–13 sessions (**Supplementary Fig. 1d**). All imaging data underwent a detailed motion-correction protocol (see Online Methods, **Supplementary Figs. 2** and **3**, and **Supplementary Videos 2** and **3**) that was similar to established methods[33].

We observed broad-based suppression of neural responses to both the target and foil tones during the active context in a majority of neurons we imaged (**Fig. 2a–d**, $n = 135/227$ target-responsive cells, $n = 146/210$ foil-responsive cells; neurons were tested for responsiveness by comparing tone-evoked response to baseline values, $P < 0.05$, Student's paired two-tailed t-test), consistent with previous extracellular recordings[1,2,9]. Surprisingly, some neurons showed an increase in activity during the task as compared to their activity in the passive context (**Fig. 2b–d**, $n = 92/227$ target-responsive cells, $n = 64/210$ foil-responsive cells, $P < 0.05$ for responsiveness per neuron, Student's paired two-tailed t-test). A continuum of context-dependent changes, from suppression to facilitation, was clearly detectable across animals (**Fig. 2e**; $P < 0.001$, Kolmogorov-Smirnov test). The continuum from broad suppression to selective facilitation was also apparent when we restricted GCaMP6s expression to excitatory neurons (**Fig. 2f–h**; $n = 620$ neurons, $n = 142$ responsive, 67% suppressed, 33% activated in the active context).

Neurons responsive to either the target or the foil tones showed a similar modulation by behavioral context (median context modulation

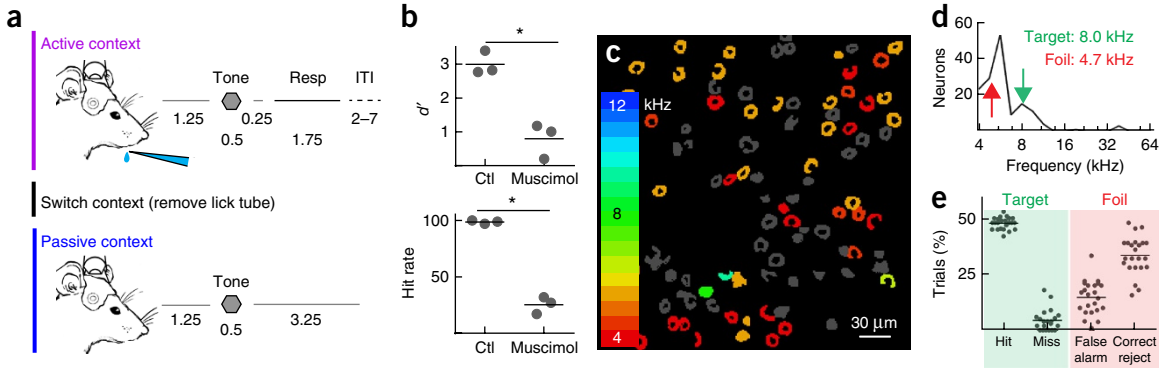

Figure 1 Task design and auditory cue selection. (**a**) Behavioral schematic showing trial structure. In the active context, pure tones are played for 0.5 s at 70 db SPL, followed by a 0.25-s grace period and a 1.75-s response window. The inter-trial interval (ITI) varied depending on behavioral outcome, with false alarms eliciting a 4-s time-out. In the passive context, the target and foil tones were played in a pseudo-random sequence with other pure tones (500 ms, 70 db SPL). There was no punishment for licking in the passive context (i.e., the absence of licking was completely voluntary). (**b**) Schematic of bilateral muscimol inactivation (1 µl of 1 mg/ml muscimol). Muscimol inactivation severely impaired behavioral performance ($d' = 3.0 \pm 0.2$, muscimol $d' = 0.8 \pm 0.3\%$, mean ± s.e.m., $n = 3$ animals, Student's paired two-tailed t-test, $t(2) = 7.733$, $P = 0.0163$; hit rate = 98.7 ± 0.9, muscimol hit rate = 25.3 ± 4.4%, mean ± s.e.m., $n = 3$ animals, Student's paired two-tailed t-test, $t(2) = 20.79$, $P = 0.0023$). (**c**) Example field of view for two-photon Ca^{2+} imaging of tone-evoked activity in A1 of an awake mouse. Color indicates best frequency of each neuron. Gray, neurons that did not significantly respond to any tones played for baseline mapping between 4 and 64 kHz. Note consistent low-frequency tuning in this field of view. (**d**) Best-frequency histogram (number of neurons with a certain best frequency). For this animal, the target was chosen to be 8 kHz (green arrow) and the foil chosen to be 4.7 kHz (red arrow). (**e**) Summary of behavioral performance in 23 trained mice (hits 47.2 ± 0.9%, misses 4.2 ± 0.9%, false alarms 15.2 ± 1.7%, correct rejects 33.9 ± 1.6%; mean ± s.e.m.).

© 2017 Nature America, Inc., part of Springer Nature. All rights reserved.

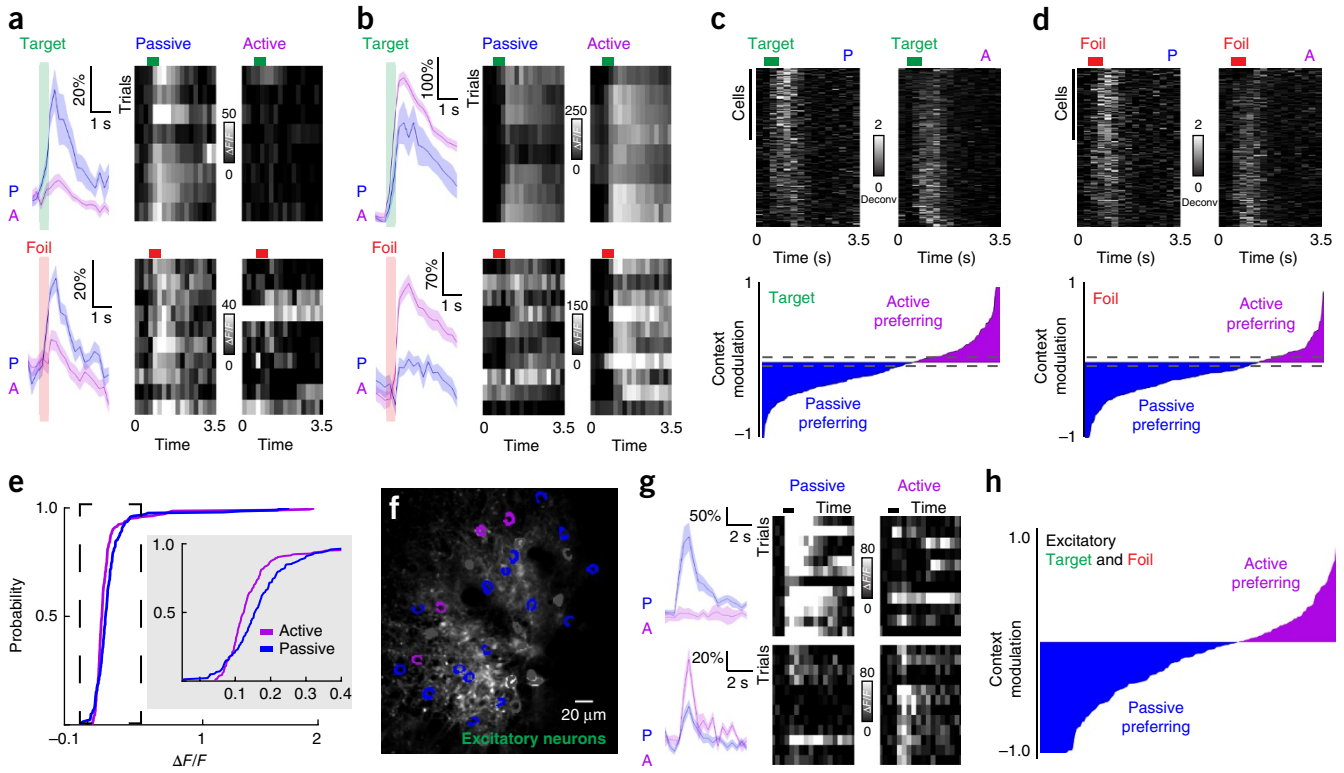

Figure 2 Task engagement elicits suppression and facilitation of A1 neurons. (**a**) Two example neurons (top, target tone responsive, $\Delta F/F = 38 \pm 6\%$, passive, $11 \pm 2\%$, active; bottom, foil tone responsive, $\Delta F/F = 29 \pm 3\%$, passive, $14 \pm 2\%$, active, mean ± s.e.m.) from the same mouse showing suppression in the active context (left, traces and shading indicate mean ± s.e.m.; right, 10-trial heatmap showing only correct trials, which include hits and correct rejects). Green and red horizontal bars indicate time of target or foil tone presentation, respectively. (**b**) Two example neurons showing elevated tone-evoked responses in the active context (top, target tone responsive, $\Delta F/F = 156 \pm 13\%$, passive, $200 \pm 2\%$, active; bottom, foil tone responsive, $\Delta F/F = 40 \pm 4\%$, passive, $96 \pm 3\%$, active, mean ± s.e.m.) in the active context (left, mean ± s.e.m.; right, 10 correct trials). (**c**) Putative spiking activity from deconvolved calcium signals of all target-responsive neurons, correct trials only in active context. Top, cells ($n = 227$ from 5 animals) sorted from most suppressed to most activated when the context was switched from passive ('P') to active ('A'). Bottom, modulation index for target-responsive neurons. Dashed lines indicate the 95% CI of a shuffled distribution. (**d**) Deconvolved spiking activity for foil-responsive neurons, correct trials only in active context. Top, cells ($n = 210$ from 5 animals) sorted from most suppressed to most activated in the active context. Bottom, modulation index for foil-responsive neurons. Dashed lines indicate the 95% CI of a shuffled distribution. (**e**) Cumulative distribution of mean tone-evoked responses for the active and passive contexts ($n = 227$ cells, $P = 0.0009$, Kolmogorov-Smirnov test). (**f**) Example images of GCaMP6s expressed specifically in excitatory neurons. Purple shading denotes neurons facilitated during behavior; blue shading, neurons suppressed during behavior; gray neurons showed no significant contextual modulation. (**g**) Example of passive-context-preferring excitatory neuron (top) and an active-context-preferring neuron (bottom); mean ± s.e.m. (**h**) Context modulation for all tone-responsive excitatory neurons ($n = 142$ cells from 5 animals, correct trials only).

for target tones −13.8 ± 4.8%, context modulation for foils −16.8 ± 4.0%, median ± 95% confidence intervals (95% CI), **Figure 2c**,**d**, bottom; dashed lines denote 95% CI generated from a shuffled data set). This indicates that task-related modulation was not due to expectation of reward on a given trial or delivery of water. Changes in neural activity occurred rapidly, within 1–2 trials of context switching (**Supplementary Fig. 4**), supporting the existence of an ensemble-level switch. Neurons whose best frequency was close to that of either the target or the foil (best frequency <0.25 octaves from target or foil; target, $n = 51$ cells, foil, $n = 24$ cells) were most likely to be suppressed during the active context (**Supplementary Fig. 5**). Conversely, neurons with best frequencies that were further from the target or foil (best frequency ≥0.25 octaves from target and foil) were more likely to be more responsive during the active context (**Supplementary Fig. 5**). Thus, behavioral context rapidly alters A1 responses, leading to a continuum of response suppression and facilitation.

Cell-type-specific activity profiles in auditory cortex

The activity of diverse inhibitory subpopulations may have a key role in generating the network output phenotype of both suppression and facilitation. We focused on the three interneuron subtypes that make up ~80% of cortical interneurons: PV$^+$, SOM$^+$ and VIP$^+$ interneurons (expressing parvalbumin, somatostatin, or vasoactive intestinal peptide, respectively)[35]. These three interneuron subtypes are thought to make up a canonical cortical circuit[7,31,36,37]. To examine the responses of inhibitory cells, we expressed GCaMP6s in *PV-tdTomato, SOM-tdTomato*, or *VIP-tdTomato* mice in order to co-localize the green calcium-sensitive signal to neurons expressing the red-fluorescent tdTomato and imaged 65 PV$^+$, 159 SOM$^+$ and 90 VIP$^+$ layer 2/3 interneurons in A1 during active and passive contexts (**Fig. 3**; cell inclusion approach in **Supplementary Fig. 6**). In contrast to those in the excitatory pool (**Fig. 3b**), inhibitory neurons showed robust change in baseline activity, with VIP$^+$ interneurons showing the largest changes, followed by SOM$^+$ and then PV$^+$ interneurons (**Fig. 3b**). Tone-evoked responses were also modulated in all subtypes, revealing that PV$^+$ and SOM$^+$ interneurons (**Fig. 3c–f**) preferred the active context, unlike those in the excitatory pool (**Fig. 3c**,**d**; 'PV$^+$', $n = 31$ tone-responsive PV$^+$ interneurons, 19/31 increased activity, $P < 0.01$ by Fisher's exact test as compared to the excitatory pool, where 47/142 had

© 2017 Nature America, Inc., part of Springer Nature. All rights reserved.

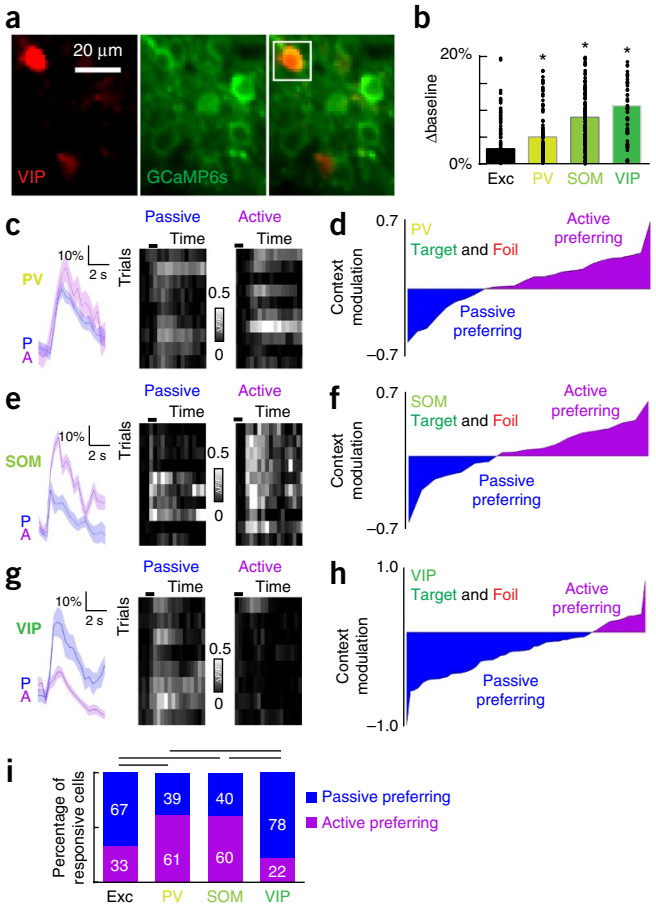

Figure 3 Contextual modulation of inhibitory neurons. (**a**) Example images of GCaMP6s (green) expressed in VIP$^+$ interneurons. (**b**) Comparison of trial-by-trial baseline calcium signal modulation across cell types (n = 144 excitatory neurons, n = 94 PV$^+$ neurons, n = 159 SOM$^+$ neurons, n = 79 VIP$^+$ neurons, one-way ANOVA, $F(3,472) = 14.97$, $P < 0.0001$; $P < 0.05$ in comparison to excitatory neurons for all cell types (*), Tukey's *post hoc* test). Baseline levels were computed as the non-evoked calcium levels either before or after tone-evoked responses. (**c**) Example of increased activity in PV$^+$ interneuron during the active context, correct trials only (mean ± s.e.m.). (**d**) Modulation index for all tone-responsive PV$^+$ interneurons (n = 31 cells, correct trials only, P = 0.0065, Fisher's exact test). (**e**) Example of increased activity in SOM$^+$ interneuron during the active context, correct trials only (mean ± s.e.m.). (**f**) Modulation index for all tone-responsive SOM$^+$ interneurons (n = 20 cells, correct trials only, P = 0.0335, Fisher's exact test). (**g**) Example of decreased activity in VIP$^+$ interneuron during the active context (mean ± s.e.m.). (**h**) Modulation index for all tone-responsive VIP$^+$ interneurons (n = 36 neurons, correct trials only, P = 0.0407, Fisher's exact test). (**i**) Comparison of context preference for each neuronal subtype ($P < 0.05$ for excitatory pool (n = 437 neurons) versus PV$^+$ and SOM$^+$, PV$^+$ versus VIP$^+$, and SOM$^+$ versus VIP$^+$, Kruskal-Wallis test with Dunn's *post hoc* test).

increased activity; **Fig. 3e**,**f**, 'SOM$^+$', n = 20 tone-responsive SOM$^+$ interneurons, 12/20 increased activity, $P < 0.01$ by Fisher's exact test as compared to excitatory pool, where 47/142 increased activity). While VIP$^+$ interneurons showed the strongest baseline modulation, tone-evoked responses from VIP$^+$ interneurons were muted in comparison and preferred the passive context, similar to excitatory neurons (**Fig. 3g**,**h**). Thus, cortical interneurons are highly sensitive to behavioral context in unique ways, suggesting that local inhibition may gate contextual information.

Synaptic inhibition acts as a switch to gate the flow of contextual information

Given the context-dependent neural output dynamics observed in inhibitory and excitatory networks, we wondered whether changes in excitatory–inhibitory balance might underlie the shifts in network activity. Balanced inhibition helps to control overall excitability and information processing. It may be a general property of developed cortical circuits in the auditory system[20,24,26] and other sensory modalities[23,35]. Co-tuning of inhibition with excitation may be disrupted in epochs of high attention or arousal and may differentially affect inhibitory transmission or inhibitory neuron activity[25,34,38–40]. Behavioral context might modulate both tone-evoked excitation and inhibition in the same direction (increasing or decreasing excitatory and inhibitory inputs together). Alternatively, changes in context might transiently disrupt excitatory–inhibitory balance, enhancing perceptual salience by selective modulation of either excitation or inhibition.

We tested these hypotheses by measuring synaptic activity onto putative excitatory neurons with whole-cell voltage-clamp recordings in behaving animals (**Fig. 4a**). We measured excitatory and inhibitory postsynaptic currents (EPSCs and IPSCs) in both the active and passive contexts (n = 12 cells, n = 4 mice). We observed significantly more context-dependent changes in IPSCs than EPSCs (**Fig. 4b**–**e**). Interestingly, the sign of inhibitory modulation was heterogeneous. In some cells, the active context enhanced tone-evoked inhibition (**Fig. 4b**–**d**), whereas inhibition was decreased in other cells, with an overall broader distribution of inhibitory changes (**Fig. 4d**). Comparing the absolute values of inhibitory versus excitatory changes revealed that during the active context, IPSC amplitudes were affected more than twice as strongly as EPSC amplitudes (**Fig. 4e**, ΔIPSC: 34.9 ± 4.1%, ΔEPSC: 16.1 ± 3.5%, n = 12 cells, $P < 0.009$, Student's paired two-tailed t-test; green circles denote significant changes in currents; ΔIPSC median P value per cell 0.03, ΔEPSC median P value 0.30, Student's paired two-tailed t-test within neuron). Tone-evoked EPSCs and IPSCs in behaving animals could be measured before the onset of licking, providing further evidence that motor-related suppression was not confounding our experiments.

We predicted firing rates using an integrate-and-fire model with our measured IPSCs and EPSCs. We observed both functional classes of neurons (activated and suppressed) that we observed with calcium imaging (**Supplementary Fig. 7a**–**c**, n = 5 neurons showing suppression, $P < 0.01$, two-sided Wilcoxon rank–sum test for active versus passive context; **Supplementary Fig. 7d**–**f**, n = 2 neurons showing activation, $P < 0.01$, two-sided Wilcoxon rank–sum test; n = 5 neurons with no significant change in model-derived spiking). In two instances, we were able to record spiking activity in cell-attached configuration in the same cells in which we later measured IPSCs and EPSCs after breaking in (**Supplementary Fig. 7g**–**i**). In both cases, the IPSC context modulation governed whether neuronal spiking was suppressed (**Supplementary Fig. 7h**) or activated (**Supplementary Fig. 7i**) in the active context. Moreover, the measured spiking output (**Supplementary Fig. 7g**–**i**, top row) was similar to the predicted spiking output calculated from the synaptic measurements (**Supplementary Fig. 7g**–**i**, bottom row), validating the model output. Overall, changes in inhibition can explain both response facilitation and suppression in excitatory output.

Optical inactivation of inhibitory subtypes impairs context-dependent switching

We next asked how the different elements of the inhibitory networks contribute to the context-dependent modulation between active and

© 2017 Nature America, Inc., part of Springer Nature. All rights reserved.

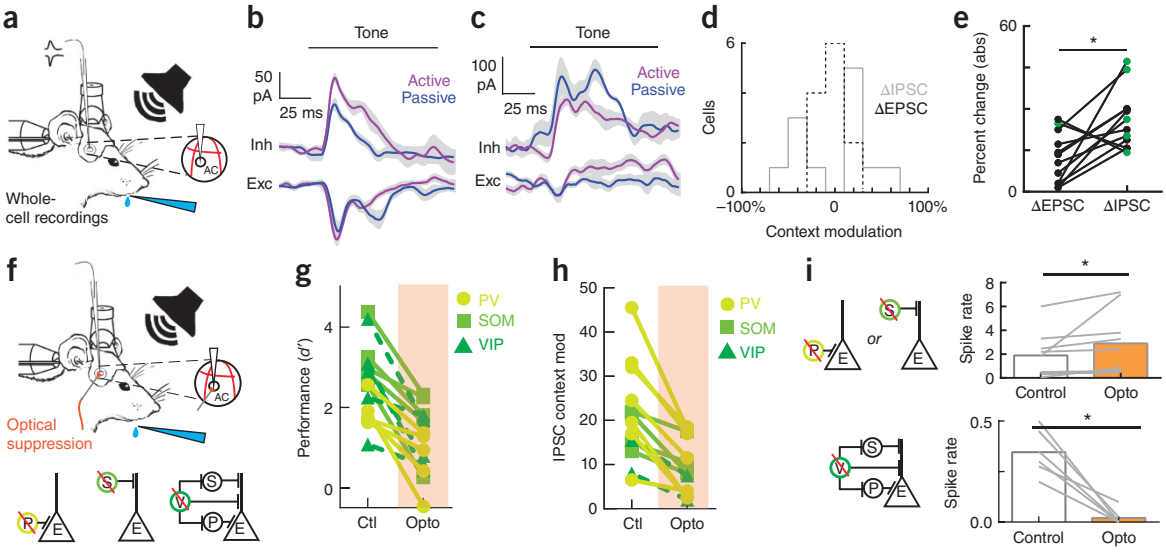

Figure 4 Inhibition acts as a synaptic switch when changing contexts. (**a**) Schematic of whole-cell recording experiments during behavior with exposed hole in cranial window for electrode access. (**b**) An example cell showing greater change in inhibitory peak (34.9%) than excitation peak (9.4%) when switching contexts (mean ± s.e.m.). (**c**) An example cell showing a large change in inhibition (40.0%) as compared to excitation (15.5%) when switching contexts (mean ± s.e.m.). (**d**) Histograms of changes in inhibition and excitation for all neurons ($n = 12$ neurons, $n = 4$ mice). (**e**) Magnitude (absolute value) of inhibitory and excitatory changes in active versus passive contexts for all neurons (ΔIPSC 34.9 ± 4.1%, ΔEPSC 16.1 ± 3.5%, mean ± s.e.m., $n = 12$ cells, Student's paired two-tailed t-test, $t(11) = 3.242$, $P = 0.0079$ (*); green circles denote significant context-dependent changes in currents within neuron, $P < 0.05$, Student's paired two-tailed t-test). (**f**) Schematic of whole-cell recording experiments during behavior and optogenetic illumination. Circuit diagrams indicating inactivation of each interneuron subtype in separate experiments (optical suppression begins 100 ms before tone onset and continues for 100 ms after tone offset). (**g**) Behavioral performance with and without optical suppression of PV, SOM or VIP interneurons (all: $n = 15$ animals, control $d' = 2.6 \pm 0.2$, opto $d' = 1.1 \pm 0.2$, Student's paired two-tailed t-test, $t(14) = 6.999$, $P < 0.0001$; 'PV': $n = 5$ animals, control $d' = 1.9 \pm 0.2$, opto $d' = 0.7 \pm 0.3$, Student's paired two-tailed t-test, $t(4) = 3.5736$, $P = 0.0233$; 'SOM': $n = 5$ animals, control $d' = 3.2 \pm 0.3$, opto $d' = 1.7 \pm 0.4$, Student's paired two-tailed t-test, $t(4) = 5.3464$, $P = 0.0059$; 'VIP': $n = 5$ animals, control $d' = 2.7 \pm 0.5$, opto $d' = 1.1 \pm 0.3$), Student's paired two-tailed t-test, $t(4) = 3.3833$, $P = 0.0277$. (**h**) Summary of whole-cell voltage clamp recordings (all: $n = 13$ neurons in 8 mice, ΔIPSC(control) 42.0 ± 6.0%, ΔIPSC(opto) 19.6 ± 3.5%, Student's paired two-tailed t-test, $t(12) = 5.764$, $P < 0.0001$; 'PV$^+$': $n = 7$ neurons in 3 mice, ΔIPSC(control) 50.8 ± 9.7%, ΔIPSC(opto) 21.1 ± 5.6%, Student's paired two-tailed t-test, $t(6) = 5.350$, $P = 0.0017$; 'SOM$^+$': $n = 5$ neurons, ΔIPSC(control) 30.7 ± 6.1%, ΔIPSC(opto) 23.6 ± 3.7%, Student's paired two-tailed t-test, $t(4) = 3.109$, $P = 0.0529$; VIP: $n = 2$ neurons, ΔIPSC(control) 23.5 ± 7.5%, ΔIPSC(opto) 9.3 ± 5.4%, Student's paired two-tailed t-test, $t(1) = 7.003$, $P = 0.0903$). (**i**) Top, optical suppression of PV$^+$ or SOM$^+$ interneurons increases pyramidal spiking in the active context (control = 1.9 ± 0.6 spikes per bin, opto = 2.9 ± 0.9 spikes per bin, Wilcoxon signed-rank test, $P = 0.0039$, $n = 5$ neurons with SOM$^+$ inactivation (Wilcoxon signed-rank test, $P = 0.0039$) and $n = 4$ neurons with PV$^+$ inactivation (Wilcoxon signed-rank test, $P = 0.0313$)). Bottom, optical suppression of VIP$^+$ interneurons reduces pyramidal spiking in the active context (control = 0.34 ± 0.05 spikes per bin, opto = 0.02 ± 0.02 spikes per bin, Wilcoxon signed-rank test, $P = 0.0313$, $n = 6$ neurons). *$P < 0.05$.

passive contexts, employing an optogenetic inactivation strategy (**Fig. 4f–i**). We expressed the hyperpolarizing opsin (eNpHR3.0) in a Cre-dependent manner in *PV-Cre*, *SOM-Cre*, and *VIP-Cre* mice to isolate the effects of each specific interneuron type in auditory cortex unilaterally.

Interestingly, optical suppression via cortical illumination of all three interneuron subtypes significantly impaired context-dependent changes in IPSCs and ultimately behavioral performance in the active context (**Fig. 4g**,**h** and **Supplementary Fig. 8b**), implicating all three in contextual regulation. Importantly, the neuronal subtypes differed in their downstream effect on pyramidal neurons. Suppression of PV$^+$ and SOM$^+$ interneurons in the active context increased pyramidal neuron spiking in the active context while reducing spiking modulation between contexts (**Fig. 4i**, top; +53.4 ± 31%, $P < 0.01$, Wilcoxon signed-rank test, $n = 9$ total (5 neurons with SOM$^+$ inactivation and 4 neurons with PV$^+$ inactivation). In contrast, suppressing VIP$^+$ interneurons in the active context strongly decreased pyramidal neuron output (**Fig. 4i**, bottom; −93.0 ± 6%, $P < 0.01$, Wilcoxon signed-rank test, $n = 6$ neurons). PV$^+$ and SOM$^+$ interneurons thus appear to directly inhibit pyramidal neurons, whereas VIP$^+$ interneurons disinhibit pyramidal neurons, during active task engagement, suggesting that multiple interneurons operate in parallel to achieve the observed network output.

Cholinergic tone signals a transition to the active context

Next we asked how behavioral context was initially communicated to A1 for control of network output in this complex manner. Cholinergic modulation from the nucleus basalis is a likely candidate for providing attentional signals to the auditory cortex[25,28,38,40–45], implicated in theoretical models[34,39] and shown experimentally to selectively control cortical inhibition under certain conditions[6,25,40].

To determine how these neuromodulatory signals are regulated by behavioral context, we measured the activity of 1,600 axonal segments, including putative boutons, arising from the nucleus basalis and projecting to auditory cortex. We targeted GCaMP6s to nucleus basalis in two wild-type mice and three *ChAT-Cre* mice to specifically target cholinergic neurons (**Fig. 5a–c** and **Supplementary Fig. 9a–e**). We monitored axonal activity in auditory cortex in behaving mice using two-photon calcium imaging (**Supplementary Video 4**). To ensure motion stability, we restricted our analysis to epochs of time (10–20 s or 40–80 frames) in which the movement in the x–y plane was similar between the active and passive contexts. We observed clear changes in baseline activity levels of axon segments from the nucleus basalis only when switching contexts (**Fig. 5b–e**, $P < 10^{-4}$ within-animal comparing active to passive context baseline calcium levels, Student's paired two-tailed t-test). During the active context, there was a substantial

© 2017 Nature America, Inc., part of Springer Nature. All rights reserved.

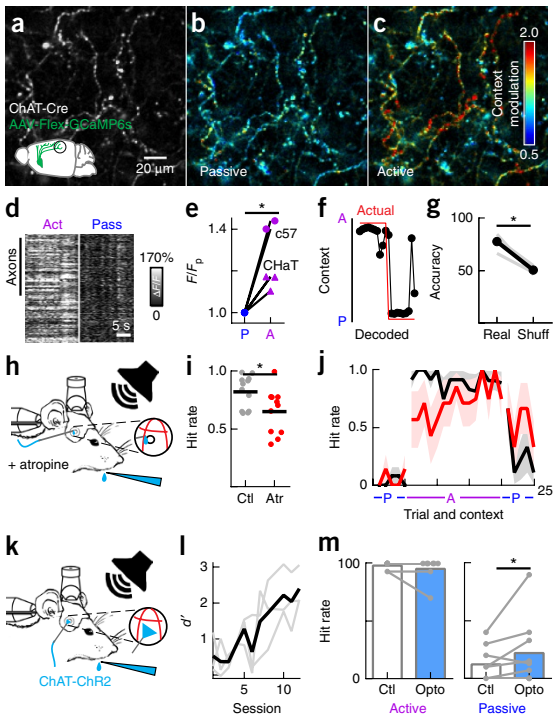

Figure 5 Cholinergic activity is necessary and partially sufficient to control behavior via inhibitory networks. (**a**) Grayscale image of cholinergic axon segments in a *ChAT-Cre* mouse. (**b**,**c**) Image from **a** pseudocolored to show differences in activity between two adjacent epochs of passive context behavior (**b**) and between two adjacent epochs (switching from active to passive) (**c**). (**d**) Axonal segments from one mouse. Each row represents the responses of one axon segment, where the grayscale indicates $\Delta F/F$ across contexts ($n = 333$ axon segments). (**e**) Comparison of overall activity levels in the active versus passive context across animals (*ChAT-Cre*: $n = 3$ mice, $n = 542$ cholinergic axon segments, $P < 0.0001$ intra-animal, Student's paired two-tailed *t*-test; inter-animal, Student's paired two-tailed *t*-test, $t(2) = 7.321$, $P = 0.0181$; c57: $n = 2$ mice, $n = 1{,}058$ axon segments, $P < 0.0001$ intra-animal, Student's paired two-tailed *t*-test). (**f**) Performance of a Bayesian decoder on the axons shown in **a**–**c**. Red line denotes actual position of lick tube and the associated behavioral context, and the black circles and line indicate the decoded lick tube position based solely on the cholinergic signal. (**g**) Summary of decoding performance across animals and sites (Predicted: 77.9 ± 3.9%, Shuffled: 50.6 ± 2.0%, $n = 4$ sites in 3 animals, Student's paired two-tailed *t*-test, $t(3) = 6.394$, $P = 0.0077$). (**h**) Behavioral schematic showing local unilateral application of atropine during behavior. (**i**) Hit rate for unilateral application over auditory cortex (atropine hit rate 0.65 ± 0.06 in 11 sessions, saline hit rate 0.82 ± 0.04 in 12 sessions, Student's unpaired two-tailed *t*-test, $t(21) = 2.439$, $P = 0.0237$, $n = 12$ control sessions; $n = 11$ sessions with unilateral application of atropine to auditory cortex). (**j**) In control conditions, when transitioning to the active context, the hit rate immediately reached steady state (first trial hit rate = 92 ± 8%, steady state = 90 ± 1.8%, $P = 0.85$, Wilcoxon signed-rank test when comparing hit rate for trials 1–4 in the active context versus trials 11–14). In atropine conditions, the animal's hit rate started significantly lower before reaching steady state (first trial hit rate = 57.1 ± 20.2%, steady state = 80.6 ± 4.0%, $P = 0.03$, Wilcoxon signed-rank test when comparing hit rate for trials 1–4 in the active context versus trials 11–14). Shading is mean ± s.e.m. (**k**) Behavioral schematic showing optical illumination of auditory cortex during behavior. (**l**) ChAT-ChR2 animals can learn the active context behavioral task within the same time frame as other genotypes ($n = 3$ mice, trained $d' = 3.1 \pm 0.5$). (**m**) Left, the hit rate in the active context is not affected by optical activation of cholinergic terminals ($n = 8$ sessions in 3 mice, $P = 0.2188$, Wilcoxon signed-rank test). Right, the hit rate is significantly (~80%) elevated in the passive context during optical activation of cholinergic terminals (control: 12 ± 5%, opto: 22 ± 10%, $n = 9$ sessions in 3 mice, $P = 0.0156$, Wilcoxon signed-rank test). $^*P < 0.05$.

increase in the tonic activity of nucleus basalis axon segments (**Fig. 5d**,**e**, $n = 1{,}600$ axonal segments in 5 mice; $n = 3$ *ChAT-Cre* animals, $P < 0.02$, Student's paired two-tailed *t*-test).

If increased cholinergic modulation is critical for active task engagement, we should observe changes in cholinergic activity that predict behavioral engagement on a trial-by-trial basis. To test this, we implemented a trial-by-trial Bayesian decoder using the pre-tone baseline calcium signal in cholinergic axonal segments to predict behavioral context. We performed a twofold cross-validation by dividing our data set into non-overlapping training and test sets, repeating this process 1,000 times with random allocation of trials to either set. We achieved 77.9 ± 3.9% accuracy in predicting context from these calcium signals compared to a shuffled data set (50.6 ± 2.0%), strongly implicating cholinergic modulation in the behavior (**Fig. 5f**,**g**). Next, we tested whether our decoder could predict key trial-to-trial variables of stimulus and action. Stimulus decoding accuracy was better than chance (real data versus shuffled data) only during tone presentation and not before (**Supplementary Fig. 9f**; pre-tone, $P = 0.95$; tone, $P = 0.04$; post-tone, $P = 0.18$; Student's *t*-test), suggesting that cholinergic terminals can carry stimulus information in a time-locked manner. Surprisingly, action-decoding accuracy (licking correctly for the target tone, withholding correctly for the foil tone) was elevated even before tone onset and became significant during the tone period (**Supplementary Fig. 9g**; pre-tone, $P = 0.06$; tone, $P = 0.01$; post-tone, $P = 0.04$; Student's *t*-test), strongly implicating fluctuations in cholinergic terminal activity as a key driver of trial-by-trial fluctuations in performance.

Given these underlying neural dynamics of elevated cholinergic signaling in the active context, we next examined whether acetylcholine (ACh) receptor activation was required for task performance. Unilateral topical application of atropine impaired performance on this task by reducing hit rate (**Fig. 5h**,**i**, atropine hit rate 0.65 ± 0.06 in 11 sessions, saline hit rate 0.82 ± 0.04 in 12 sessions, $P < 0.05$, Student's paired two-tailed *t*-test, **Supplementary Fig. 9h**,**i**). Trial-by-trial analysis showed that the animal's response rate was most impaired immediately after context switches (**Fig. 5j**). In control conditions, during transition to the active context, the animal's hit rate immediately reached steady state (first trial hit rate = 92 ± 8%, steady state = 90 ± 1.8%, $P = 0.85$ Wilcoxon signed-rank test when comparing hit rate for trials 1–4 versus trials 11–14 in the active context). In atropine conditions, the animal's hit rate started significantly lower before reaching steady state (first trial hit rate = 57.1 ± 20.2%, steady state = 80.6 ± 4.0%, $P < 0.05$, Wilcoxon signed-rank test when comparing hit rate for trials 1–4 versus trials 11–14 in the active context). We next asked whether direct activation of cholinergic terminals in auditory cortex could trigger task-like behavior even in the passive context (i.e., with no lick tube present; **Fig. 5k**–**m**, **Supplementary Fig. 10**). Surprisingly, illumination of the auditory cortex in the passive context of trained animals induced tone-evoked licking. In the passive context, behavioral responses to the target tone (licking) are minimal (12 ± 5%), but they are increased ~80% during activation of cholinergic inputs to auditory cortex of trained mice (22 ± 10%) (**Fig. 5m**; $n = 9$ sessions in 3 mice, $P < 0.05$, Wilcoxon signed-rank test). This partial restoration of active-context behavior argues that the cholinergic system plays a critical role in signaling context. It is likely that other key factors, including those that continuously update the animal on the contextual environment such as water reinforcement and somatosensation of the tongue to the lick tube, counterbalance the cholinergic activation. Overall, these behavioral manipulations argue that cholinergic signaling is necessary for contextual transitions and can even partially restore task-like behavior in the passive context.

© 2017 Nature America, Inc., part of Springer Nature. All rights reserved.

Can this elevation in cholinergic tone drive the inhibitory dynamics that appear to control network output? To directly measure how this cholinergic modulation may affect layer 2/3 neurons in the auditory cortex, we performed whole-cell recordings in acute brain slices and examined the membrane potential of specific neuronal subtypes in response to a cholinergic agonist (1 μM muscarine) while blocking NMDA, AMPA, and $GABA_A$ receptors. As suggested by previous studies in mouse barrel cortex and visual cortex[38,40], inhibitory interneurons were generally more depolarized than excitatory neurons during muscarine application (**Fig. 6a–c**; $n = 19$ interneurons, $n = 15$ excitatory neurons, $P < 0.001$, Student's two-tailed t-test, spikes removed). Excitatory neurons exhibited the least depolarization of all cell types (**Fig. 6b**,**c**; $n = 15$ neurons, median depolarization 1.6 mV, interquartile range (IQR) 0–4.3 mV); PV^+ interneurons were modestly depolarized (**Fig. 6b**,**c**; PV^+: $n = 7$, +5.6 mV, IQR 5.1–9.4), while SOM^+ and VIP^+ interneurons were more strongly depolarized (**Fig. 6b**,**c**; SOM^+: $n = 7$, +8.2 mV, IQR 7.2–18.3; VIP^+: $n = 5$, +8.6 mV, IQR 3.8–9.6). These data support our calcium imaging measurements from behaving animals, given that VIP and SOM neurons exhibited the largest baseline changes in activity while PV^+ neurons experienced increases in tone-evoked responses. These results, however, do not preclude network-level effects of ACh on interneuron spiking: for example, ACh may act indirectly on interneuron spiking by modulating synaptic inputs, both excitatory and inhibitory, onto interneurons. Regardless, cholinergic modulation of cortical inhibition provides a powerful, cell-type-selective mechanism for contextual regulation of network output and behavioral control.

Cholinergic modulation drives changes in synaptic inhibition

We then examined how cholinergic modulation directly affected excitatory and inhibitory inputs during behavior. First, we made additional whole-cell voltage-clamp recordings during behavior while applying the muscarinic ACh receptor antagonist atropine (1 mM) locally to auditory cortex (**Fig. 6d–f**). Atropine significantly reduced contextual modulation of tone-evoked inhibition (**Fig. 6e**,**f**). Remarkably, six out of seven neurons did not show significant changes in IPSCs (**Fig. 6f**, ΔIPSC: 19.7 ± 5.6%, ΔEPSC: 30.3 ± 5.6%, $n = 7$ cells, $P < 0.02$, Student's paired two-tailed t-test; green circles denote significant changes in currents, $P < 0.05$, Student's two-tailed t-test within neuron). Moreover, atropine altered the timing of synaptic inputs such that the time lag between excitation and inhibition was more variable and consistently larger than in control conditions (**Supplementary Fig. 11**). Cholinergic activity therefore controls network activity by modulating the amplitude of inhibitory inputs and sharpening the timing of synaptic inputs.

If ACh is required for contextual changes in inhibition, we reasoned that direct activation of the cholinergic system should preferentially modulate inhibition. We performed whole-cell voltage-clamp recordings in awake *ChAT-ChR2* mice and optogenetically activated cholinergic terminals in A1 (**Fig. 6g–i**). Optogenetic release of endogenous ACh desynchronized cortical activity (**Supplementary Fig. 12**), and significantly altered tone-evoked inhibition to a greater extent than excitation (**Fig. 6h**,**i**). As with context switching, the sign of inhibitory context modulation was heterogeneous, even within the same cell. For example, at one frequency (13.5 kHz), optogenetic stimulation enhanced tone-evoked inhibition in a single neuron (**Fig. 6h**), while at a different frequency (26.9 kHz), optogenetic stimulation reduced tone-evoked inhibition (**Fig. 6h**). In either case, however, inhibition changed more than excitation (**Fig. 6h**,**i**). Overall IPSC amplitudes were nearly 50% more dynamic than EPSC amplitudes after optogenetic illumination (**Fig. 6i**; (IPSC: 17.8 ± 2.5%, ΔEPSC: 12.6 ± 1.7%, $n = 5$ cells, $P < 0.03$, Student's paired two-tailed t-test; green circles denote significant changes in currents, $P < 0.05$, Student's two-tailed t-test within neuron). Taken together, our results show that cholinergic switching is required in awake mice to control cortical inhibition.

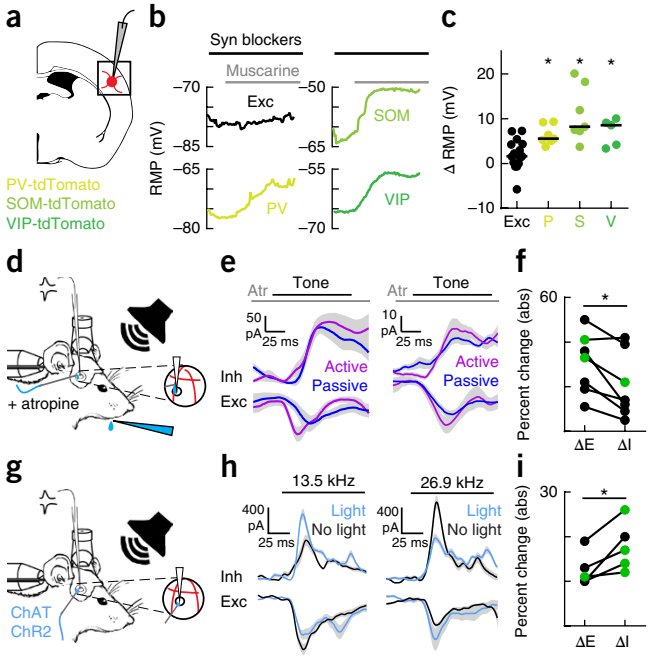

Figure 6 Cholinergic activity impacts inhibition directly. (**a**) Schematic of slice recordings in mice expressing tdTomato in either PV, SOM, or VIP interneurons. (**b**) Example *in vitro* recordings from adult mouse auditory cortex showing average resting membrane potential (RMP) in 2-s and 10-s sweeps. Please note that spikes have been removed in the SOM^+ recordings. Synaptic blockers (DNQX, APV and picrotoxin) were washed in for at least 5 min before muscarine wash-in (1–2 μM). (**c**) Summary of *in vitro* recordings showing significantly greater depolarization of cortical interneurons in comparison to excitatory neurons (overall: $n = 19$ interneurons, $n = 15$ excitatory neurons, Student's unpaired two-tailed t-test, $t(32) = 4.44$, $P = 0.0001$, spikes removed; cell-type-specific responses: PV^+: $n = 7$, median = +5.6 mV, IQR 5.1–9.4; SOM^+: $n = 7$, median = +8.2 mV, IQR 7.2–18.3; VIP^+: $n = 5$, median = +8.6 mV, IQR 3.8–9.6; one-way ANOVA, $F(4,30) = 9.015$, $P = 0.0001$; $P < 0.05$ for all interneuron subtypes versus excitatory neurons (PV: $P = 0.0218$; SOM: $P < 0.0001$; VIP: $P = 0.0182$), Tukey's *post hoc* test). (**d**) Setup for whole-cell recording with local pharmacology in behaving head-fixed mice. (**e**) Two example cells from two different animals that showed only modest contextual changes in tone-evoked IPSCs in presence of atropine (1 mM); mean ± s.e.m. (**f**) Absolute value of change in inhibition versus excitation in atropine (ΔIPSC 19.7 ± 5.6%, ΔEPSC 30.3 ± 5.6%, $n = 7$ cells, Student's paired two-tailed t-test, $t(6) = 3.3252$, $P = 0.0159$; green circles denote significant context-dependent changes in currents within neuron, $P < 0.05$, Student's paired two-tailed t-test within neuron). (**g**) Setup for whole-cell recording and optogenetics in *ChAT-ChR2* mice. (**h**) Example recordings from the same cell, showing tone-evoked responses to 13.5 kHz (left) and 26.9 kHz (right) with and without optogenetic cholinergic modulation in auditory cortex (mean ± s.e.m.). Left, 13.5 kHz responses showed greater increase in inhibitory peak (+38.8%) and integral (+23.4%) than decrease in excitatory peak (35.9%) and integral (+0.0%). Right, 26.9-kHz responses showed greater decrease in inhibitory peak (85.2%) and integral (30.0%,) than increase in excitatory peak (+35.6%) and integral (+24.3%) when optogenetic illumination was switched on and off. (**i**) Magnitude (absolute value) of inhibitory and excitatory changes between optogenetic illumination on and off for all neurons across complete tuning curve (ΔIPSC 17.8 ± 2.5%, ΔEPSC 12.6 ± 1.7%, $n = 5$ cells, Student's paired two-tailed t-test, $t(4) = 3.399$, $P = 0.0273$; green circles denote significant context-dependent changes in currents within neuron, $P < 0.05$, Student's paired two-tailed t-test within neuron). *$P < 0.05$.

© 2017 Nature America, Inc., part of Springer Nature. All rights reserved.

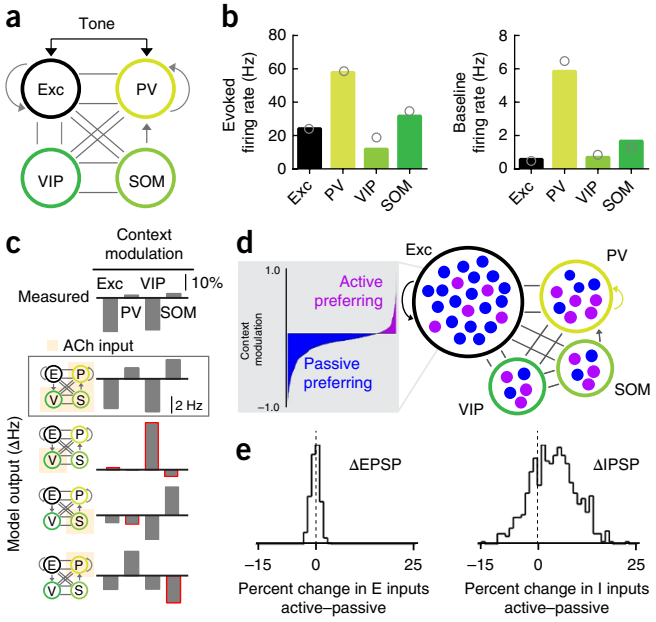

Figure 7 Network model demonstrates requirement for co-activation of inhibitory and disinhibitory circuit elements. (**a**) Schematic of the four-unit rate-based model. (**b**) Evoked and baseline firing rates of each cell type in the four-unit model. Gray circles represent experimental values derived from the literature. (**c**) Changes in activity of all subtypes due to context (Active – Passive). The top plot shows the experimental values in terms contextual modulation index. The remaining plots relate to the network model and show changes in firing rates when ACh activates PV$^+$, VIP$^+$ and SOM$^+$ populations either simultaneously (second plot) or individually (third through fifth plots). Red outlines indicate directional changes that do not match the observed direction of change. (**d**) Schematic of the multi-unit model in which each population is comprised of several rate units. The gray box shows the distribution of active- and passive-preferring excitatory cells in the model. (**e**) Histograms of the changes in synaptic inputs due to context (in terms of percent of total input in passive condition) for total excitatory (left) and inhibitory (right) input to individual E cells in the multi-unit model. Note the diversity in inhibitory inputs.

Recurrent model recapitulates network output only with parallel activation of inhibition

Our data indicate that multiple sources of inhibition are recruited in parallel by cholinergic activity to adjust input–output dynamics in the cortex. Could similar results arise from just the activation of VIP$^+$ interneurons alone, or perhaps only the PV$^+$ or SOM$^+$ subpopulations? Alternatively, appropriate switching of cortical activity might arise from multiple inhibitory and disinhibitory interactions, required to generate the observed task-related modulation while maintaining an overall level of excitatory–inhibitory balance. To examine this central question requires network modeling in order to fully explore the complex dynamics between multiple cell types and neuromodulatory signaling. Thus we built a four-population rate-based network model that incorporated known connectivity parameters across neuronal subtypes[24,25] (**Fig. 7a**). We then simulated the effects of context switching via cholinergic modulation of all inhibitory cell types. Importantly, the model recapitulated known features of cortical responses at baseline and to sensory inputs in all cell types (**Fig. 7b**; bars denote model output, circles denote measured spike rates from literature[26,28]). If the model incorporated only cholinergic activation of VIP$^+$ interneurons, the network dynamics from the model were nearly opposite to what we observed experimentally (**Fig. 7c**). Likewise, if ACh only activated SOM$^+$ or PV$^+$ interneurons, the network dynamics were similar to the mean excitatory suppression we observed experimentally, but other circuit responses were not captured (**Fig. 7c**). In contrast, if ACh acted simultaneously on all three interneuron subtypes, the model could recapitulate all key network responses and was robust to various changes in parameters (**Fig. 7c**, **Supplementary Fig. 13**).

We analyzed the model dynamics to determine how the network state was switched by change in context. These results arise, in part, because of the interconnectivity between interneuron subtypes. For example, cholinergic activation of PV$^+$ neurons alone suppresses excitatory and VIP neurons, but also incorrectly suppresses SOM$^+$ neurons. Activation of PV$^+$ and SOM$^+$ neurons together overcomes the mutual suppression but leads to direct suppression of VIP even at baseline. Activation of all three in parallel, however, creates the right balance for all three subtypes for both tone-evoked and baseline activity levels. A multi-unit rate model generated excitatory diversity about a mean suppression, including neurons with robust facilitation due to the diffuse nature of the ACh signal and the underlying stochastic connectivity properties (**Fig. 7d**). Importantly, this diversity emerged largely as the result of diverse changes in inhibitory inputs (**Fig. 7e**). Together, the network model provides strong theoretical foundation for parallel processing by cortical interneurons of neuromodulatory signals during behavior.

DISCUSSION

A major challenge in neural systems is to provide logic to complex neural dynamics. We present a cohesive model, based on experiments and theory, that shows how parallel processing of cholinergic modulation by diverse cortical interneurons enables the same sensory stimuli to trigger different behaviors depending on context. Surprisingly, excitatory synaptic inputs themselves are only modestly affected by context. Instead, during active engagement, cholinergic input co-activates multiple interneurons, thereby adjusting inhibitory synaptic inputs and consequently modulating neuronal output. A network model captured these dynamics across neuronal subtypes only when neuromodulation coincidently drove inhibitory and disinhibitory circuit elements, ruling out either as sole computational responses to cholinergic modulation.

Task engagement drives a continuum of responses, from suppression to facilitation, in A1

Most excitatory neurons in A1 were suppressed when the animal was engaged in the task, but many also showed response facilitation. This synthesizes findings from different research groups showing suppression during task engagement[2] and different forms of facilitation[3,4]. The behavioral significance of this bidirectional modulation remains an important question. During locomotion, neuronal responses to auditory stimuli are systematically suppressed, with no facilitation in the auditory cortex and the auditory thalamus[12,17,46]. Moreover, while thalamic neurons exhibit locomotion-induced suppression, they are less sensitive to task engagement with higher cognitive load[2,12]. Thus, facilitation of a pool of excitatory neurons appears to be cortical in nature, independent of processing earlier in the auditory pathway, and may be critical for task performance.

Imaging of inhibitory networks in the cortex demonstrated the diversity of responses both within and across interneuron sub-types. PV$^+$ and SOM$^+$ interneurons preferred the active context at baseline and for tone-evoked responses. In contrast, VIP$^+$ interneurons showed large, uniform increases in baseline activity but exhibited suppressed tone-evoked responses in the active context. This suggests

© 2017 Nature America, Inc., part of Springer Nature. All rights reserved.

that inhibitory networks regulate cortical output at both a tonic and a phasic level. These results are consistent with these three interneuron subtypes being sensitive to cholinergic regulation and having strong levels of interconnectivity[6,31,47]. Most importantly, it suggests that multiple interneurons are involved in regulating cortical activity during the active context.

Inhibition as a synaptic switch to control network output and context-dependent behavior

Direct recording of synaptic inputs onto single neurons during behavior is a powerful approach to dissect input–output dynamics. Our data show that inhibitory inputs were more sensitive to changes in behavioral context than excitatory inputs, under the control of cholinergic neuromodulation in a context-switching behavioral paradigm. Optical suppression of PV^+ and SOM^+ neurons during active behavior increased layer 2/3 pyramidal neuron output, implicating these neurons in the suppression of excitatory output. In contrast, optical suppression of VIP^+ interneurons during active behavior decreased layer 2/3 pyramidal output, implicating these neurons in disinhibition. Moreover, unilateral optogenetic suppression of any of these interneurons reduced the strength of contextual modulation of IPSCs and impaired task performance. This shows that multiple interneurons play a key role in gating contextual information.

Cholinergic signaling activates multiple interneurons in parallel during behavior

Task engagement was conveyed to the cortex by the cholinergic projections of the nucleus basalis. Calcium imaging of neuromodulatory axons in recipient regions, such as the auditory cortex, allows us to better understand how neuromodulatory systems selectively engage during behaviorally relevant epochs. In the context-switching behavioral paradigm, the activity of cholinergic axons from the nucleus basalis increased during task engagement. We showed in cortical brain slices that a cholinergic agonist (muscarine) depolarized inhibitory interneurons significantly more than excitatory neurons. Our data do not preclude the possibility that other basal forebrain projections that release GABA, glutamate, or peptides may also show differences in activity[48]. However, we note that blocking cortical muscarinic ACh receptors reduced changes in IPSCs and impaired behavioral performance, suggesting that cholinergic modulation of synaptic inhibition is critical for control of cortical state. Moreover, tone-evoked licking could be partially recovered in the passive context by optically activating cholinergic axons in the auditory cortex of trained mice. Our focus has been on the activation of muscarinic receptors in cortical neurons. A complementary and important future avenue of work will further dissect the role of nicotinic receptor activation. This further dissection may also show that cholinergic activity may impact other important mechanisms for task-related responses, including modulation of thalamocortical activity[49].

These findings complement recent work showing how phasic responses of cholinergic neurons[30]. It is likely that the cholinergic system modulates behavior both by setting the contextual tone and by providing rapid phasic signals during behavior[30]. Our findings, however, do not preclude a role for other neuromodulatory centers or long-range cortical connections from influencing context-dependent activity in auditory cortex. In addition, basal forebrain projections to the visual cortex have been shown to yield opposite direction of modulation: namely, visual cortical neurons show increased activity during cholinergic stimulation[50]. These cortical differences may arise as a result of the preferential and region-specific innervation of specific subtypes of interneurons[7,31]. Moreover, it is likely that other key neuromodulatory centers may be critical for maintaining full performance. Other circuits may impinge on cortical circuits to further influence this switching time as well as steady-state performance. Overall, these results show how cortical inputs and outputs are transformed by behavioral context. Parallel processing by diverse cortical interneurons of long-range inputs may therefore be a general feature of cortical activity during cognitive behaviors.

METHODS

Methods, including statements of data availability and any associated accession codes and references, are available in the online version of the paper.

Note: Any Supplementary Information and Source Data files are available in the online version of the paper.

ACKNOWLEDGMENTS

We thank I. Carcea, G. Fishell, B. Kripkee, M. Long, M. Picardo, D. Rinberg, R. Tsien, and D. Vallentin for comments on earlier versions of this manuscript; K. Katlowitz, X. Lin, H. Lu, J. Merel, and L. Paniniski for assistance with statistics and analysis; and G. Kosche, E. Morina, A. Resulaj, and C. Wilson for technical assistance. Artwork in **Figures 1**, **4**, **5** and **6** was made by S.E. Ross. We thank the GENIE Program and the Janelia Farm Research Campus, Howard Hughes Medical Institute for provision of GCaMP6s and ScanImage. Artwork in Figures 1, 4, and 6 was made by S.E. Ross. This work was funded by grants from the NIDCD (DC009635 and DC012557), a Sloan Research Fellowship, and a Klingenstein Fellowship (R.C.F.) and by a grant from the NIDA (T32 DA007254), the Charles H. Revson Senior Fellowship in Biomedical Sciences, and a grant from the NIDCD (DC05014) (K.V.K.).

AUTHOR CONTRIBUTIONS

K.V.K. and R.C.F. designed experiments and wrote the manuscript. K.V.K., J.V.G., R.E.F., and E.S.P. conducted experiments. K.V.K., T.A.H.S., and J.V.G. performed analysis. G.W.L. and K.D.M. performed network modeling.

COMPETING FINANCIAL INTERESTS

The authors declare no competing financial interests.

Reprints and permissions information is available online at http://www.nature.com/reprints/index.html.

1. Fritz, J., Shamma, S., Elhilali, M. & Klein, D. Rapid task-related plasticity of spectrotemporal receptive fields in primary auditory cortex. *Nat. Neurosci.* **6**, 1216–1223 (2003).
2. Otazu, G.H., Tai, L.H., Yang, Y. & Zador, A.M. Engaging in an auditory task suppresses responses in auditory cortex. *Nat. Neurosci.* **12**, 646–654 (2009).
3. Atiani, S. *et al.* Emergent selectivity for task-relevant stimuli in higher-order auditory cortex. *Neuron* **82**, 486–499 (2014).
4. Rodgers, C.C. & DeWeese, M.R. Neural correlates of task switching in prefrontal cortex and primary auditory cortex in a novel stimulus selection task for rodents. *Neuron* **82**, 1157–1170 (2014).
5. Leonard, M.K. & Chang, E.F. Dynamic speech representations in the human temporal lobe. *Trends Cogn. Sci.* **18**, 472–479 (2014).
6. Letzkus, J.J. *et al.* A disinhibitory microcircuit for associative fear learning in the auditory cortex. *Nature* **480**, 331–335 (2011).
7. Fu, Y. *et al.* A cortical circuit for gain control by behavioral state. *Cell* **156**, 1139–1152 (2014).
8. Niell, C.M. & Stryker, M.P. Modulation of visual responses by behavioral state in mouse visual cortex. *Neuron* **65**, 472–479 (2010).
9. David, S.V., Fritz, J.B. & Shamma, S.A. Task reward structure shapes rapid receptive field plasticity in auditory cortex. *Proc. Natl. Acad. Sci. USA* **109**, 2144–2149 (2012).
10. Tabossi, P. Effects of context on the immediate interpretation of unambiguous nouns. *J. Exp. Psychol. Learn.* **14**, 153–162 (1988).
11. Gennari, S.P., MacDonald, M.C., Postle, B.R. & Seidenberg, M.S. Context-dependent interpretation of words: evidence for interactive neural processes. *Neuroimage* **35**, 1278–1286 (2007).
12. Williamson, R.S., Hancock, K.E., Shinn-Cunningham, B.G. & Polley, D.B. Locomotion and task demands differentially modulate thalamic audiovisual processing during active search. *Curr. Biol.* **25**, 1885–1891 (2015).
13. Jaramillo, S., Borges, K. & Zador, A.M. Auditory thalamus and auditory cortex are equally modulated by context during flexible categorization of sounds. *J. Neurosci.* **34**, 5291–5301 (2014).
14. McGinley, M.J., David, S.V. & McCormick, D.A. Cortical membrane potential signature of optimal states for sensory signal detection. *Neuron* **87**, 179–192 (2015).

© 2017 Nature America, Inc., part of Springer Nature. All rights reserved.

15. Miller, J.M. *et al.* Single cell activity in the auditory cortex of Rhesus monkeys: behavioral dependency. *Science* **177**, 449–451 (1972).
16. Hubel, D.H., Henson, C.O., Rupert, A. & Galambos, R. Attention units in the auditory cortex. *Science* **129**, 1279–1280 (1959).
17. Zhou, M. *et al.* Scaling down of balanced excitation and inhibition by active behavioral states in auditory cortex. *Nat. Neurosci.* **17**, 841–850 (2014).
18. Kato, H.K., Gillet, S.N. & Isaacson, J.S. Flexible sensory representations in auditory cortex driven by behavioral relevance. *Neuron* **88**, 1027–1039 (2015).
19. Tan, A.Y. & Wehr, M. Balanced tone-evoked synaptic excitation and inhibition in mouse auditory cortex. *Neuroscience* **163**, 1302–1315 (2009).
20. Wehr, M. & Zador, A.M. Balanced inhibition underlies tuning and sharpens spike timing in auditory cortex. *Nature* **426**, 442–446 (2003).
21. Volkov, I.O. & Galazjuk, A.V. Formation of spike response to sound tones in cat auditory cortex neurons: interaction of excitatory and inhibitory effects. *Neuroscience* **43**, 307–321 (1991).
22. Anderson, J.S., Carandini, M. & Ferster, D. Orientation tuning of input conductance, excitation, and inhibition in cat primary visual cortex. *J. Neurophysiol.* **84**, 909–926 (2000).
23. Ferster, D. Orientation selectivity of synaptic potentials in neurons of cat primary visual cortex. *J. Neurosci.* **6**, 1284–1301 (1986).
24. Froemke, R.C. Plasticity of cortical excitatory-inhibitory balance. *Annu. Rev. Neurosci.* **38**, 195–219 (2015).
25. Froemke, R.C., Merzenich, M.M. & Schreiner, C.E. A synaptic memory trace for cortical receptive field plasticity. *Nature* **450**, 425–429 (2007).
26. Marlin, B.J., Mitre, M., D'amour, J.A., Chao, M.V. & Froemke, R.C. Oxytocin enables maternal behaviour by balancing cortical inhibition. *Nature* **520**, 499–504 (2015).
27. Kuhlman, S.J. *et al.* A disinhibitory microcircuit initiates critical-period plasticity in the visual cortex. *Nature* **501**, 543–546 (2013).
28. Bakin, J.S. & Weinberger, N.M. Induction of a physiological memory in the cerebral cortex by stimulation of the nucleus basalis. *Proc. Natl. Acad. Sci. USA* **93**, 11219–11224 (1996).
29. Kilgard, M.P. & Merzenich, M.M. Cortical map reorganization enabled by nucleus basalis activity. *Science* **279**, 1714–1718 (1998).
30. Hangya, B., Ranade, S.P., Lorenc, M. & Kepecs, A. Central cholinergic neurons are rapidly recruited by reinforcement feedback. *Cell* **162**, 1155–1168 (2015).
31. Pi, H.J. *et al.* Cortical interneurons that specialize in disinhibitory control. *Nature* **503**, 521–524 (2013).
32. Chubykin, A.A., Roach, E.B., Bear, M.F. & Shuler, M.G. A cholinergic mechanism for reward timing within primary visual cortex. *Neuron* **77**, 723–735 (2013).
33. Lovett-Barron, M. *et al.* Dendritic inhibition in the hippocampus supports fear learning. *Science* **343**, 857–863 (2014).
34. Vogels, T.P. & Abbott, L.F. Gating multiple signals through detailed balance of excitation and inhibition in spiking networks. *Nat. Neurosci.* **12**, 483–491 (2009).
35. Rudy, B., Fishell, G., Lee, S. & Hjerling-Leffler, J. Three groups of interneurons account for nearly 100% of neocortical GABAergic neurons. *Dev. Neurobiol.* **71**, 45–61 (2011).
36. Kepecs, A. & Fishell, G. Interneuron cell types are fit to function. *Nature* **505**, 318–326 (2014).
37. Xue, M., Atallah, B.V. & Scanziani, M. Equalizing excitation-inhibition ratios across visual cortical neurons. *Nature* **511**, 596–600 (2014).
38. Xiang, Z., Huguenard, J.R. & Prince, D.A. Cholinergic switching within neocortical inhibitory networks. *Science* **281**, 985–988 (1998).
39. Hasselmo, M.E. & Bower, J.M. Acetylcholine and memory. *Trends Neurosci.* **16**, 218–222 (1993).
40. Kruglikov, I. & Rudy, B. Perisomatic GABA release and thalamocortical integration onto neocortical excitatory cells are regulated by neuromodulators. *Neuron* **58**, 911–924 (2008).
41. Froemke, R.C. *et al.* Long-term modification of cortical synapses improves sensory perception. *Nat. Neurosci.* **16**, 79–88 (2013).
42. Dorrn, A.L., Yuan, K., Barker, A.J., Schreiner, C.E. & Froemke, R.C. Developmental sensory experience balances cortical excitation and inhibition. *Nature* **465**, 932–936 (2010).
43. Metherate, R. & Weinberger, N.M. Cholinergic modulation of responses to single tones produces tone-specific receptive field alterations in cat auditory cortex. *Synapse* **6**, 133–145 (1990).
44. Pinto, L. *et al.* Fast modulation of visual perception by basal forebrain cholinergic neurons. *Nat. Neurosci.* **16**, 1857–1863 (2013).
45. Lin, S.C. & Nicolelis, M.A. Neuronal ensemble bursting in the basal forebrain encodes salience irrespective of valence. *Neuron* **59**, 138–149 (2008).
46. Schneider, D.M., Nelson, A. & Mooney, R. A synaptic and circuit basis for corollary discharge in the auditory cortex. *Nature* **513**, 189–194 (2014).
47. Lee, S., Kruglikov, I., Huang, Z.J., Fishell, G. & Rudy, B. A disinhibitory circuit mediates motor integration in the somatosensory cortex. *Nat. Neurosci.* **16**, 1662–1670 (2013).
48. Mayse, J.D., Nelson, G.M., Avila, I., Gallagher, M. & Lin, S.C. Basal forebrain neuronal inhibition enables rapid behavioral stopping. *Nat. Neurosci.* **18**, 1501–1508 (2015).
49. Kawai, H., Lazar, R. & Metherate, R. Nicotinic control of axon regulates thalamocortical transmission. *Nat. Neurosci.* **10**, 1168–1175 (2007).
50. Goard, M. & Dan, Y. Basal forebrain activation enhances cortical coding of natural scenes. *Nat. Neurosci.* **12**, 1444–1449 (2009).

© 2017 Nature America, Inc., part of Springer Nature. All rights reserved.

ONLINE METHODS

Surgical preparation. All procedures were approved under a New York University IACUC protocol. To generate PV-tdTomato, SOM-tdTomato and VIP-tdTomato mice, PV-Cre, SOM-Cre, and VIP-Cre animals were crossed with the Ai9 (Allen Institute) tdTomato-flox reporter line. ChAT-Cre mice were used for imaging cholinergic axon terminals (JAX) and ChAT-ChR2 mice were used for optogenetic experiments. C57/Bl6 mice were used in all other experiments. In all cases, male and female mice 2–3 months old were anesthetized with isoflurane (2.0% during induction and surgery, 0.75% during physiology). A craniotomy was performed over the temporal lobe to expose the auditory cortex (3 mm craniotomy, centered 1.75 mm anterior to the lambda suture on the ridge line). Pure tones at 70 dB SPL and 4–64 kHz frequencies (50 ms, 3 ms cosine on/off ramps, quarter-octave spacing) were delivered in pseudo-random sequence at 0.5–1 Hz. The location of A1 was determined by mapping multiunit responses 500–700 μm below the surface using tungsten electrodes in a sound-attenuating chamber. An adeno-associated virus (AAV) vector encoding the calcium indicator GCaMP6s (AAV1-SYN-GCAMP6s, UPENN vector core) was injected for expression in layer 2/3 neurons in right A1 (n = 5 mice for **Fig. 2a**–**e**; in **Fig. 3**, n = 2 mice for PV-tdTomato, n = 2 mice for SOM-tdTomato, and n = 2 mice for VIP-tdTomato). For isolation of excitatory neurons, we used an AAV encoding the calcium indicator GCaMP6f (AAV9.CamKII.GCaMP6f) (n = 2 mice). Above the injection coordinates, a cranial window was implanted replacing a circular piece of skull by a glass coverslip (diameter of 3 mm, Warner Instruments) that was secured in place using a mix of dental cement and Krazy Glue. A custom-made stainless-steel headpost (Ponoko) was affixed to the skull using C&B Metabond dental cement (Parkell). A small burr hole was drilled anterior to bregma and a ground wire was placed under the skull above the pial surface. The ground wire was then connected to the metal headpost to allow for lick-detection. Each animal was allowed to recover for at least 2–3 weeks.

For experiments imaging the activity of axonal projections from the basal forebrain, we carefully leveled the head and drilled a small burr hole targeting the right nucleus basalis (AP, -0.5 mm; ML, 1.8 mm; DV, 4.5 mm). We injected 1.5 μl of an AAV vector encoding the calcium indicator AAV1-SYN-GCAMP6s (University of Pennsylvania vector core) into C57 mice (JAX), or 1.5 μl of AAV1-SYN-FLEX-GCAMP6s (University of Pennsylvania vector core) into *ChAT-Cre* mice to specifically target cholinergic neurons. We injected at a rate of 100 nl/min and waited 15 min before extracting the injection needle. We filled the burr hole with bone wax and sealed it with dental cement.

Behavioral training and control for imaging experiments. All behavioral events (imaging time-stamping, stimulus delivery, water delivery, and lick detection) were monitored and controlled by custom-written programs in MATLAB interfacing with an RZ6 auditory processor (Tucker-Davis Technologies). Training began after at least 7 d of water restriction. Training took place during the day and began with habituation to head-fixation, which was immediately followed by water-sampling sessions while animals were immobilized in a Plexiglas tube. Mice typically learned to lick aggressively for 3- to 5-μl droplets of water within 1–2 sessions. Once the animals would lick reliably, they were immediately placed in the complete behavioral task with minimal shaping. We used a go/no-go behavior task with the target and foil chosen based on the two-photon targeted imaging. Importantly, the initial training session included passive context behavior (i.e., the tones but no behavioral responses), as animals would continue to lick even in the absence of the lick tube if the passive context was not introduced early in the training procedure. For active context, a behavioral block typically consisted of 100 trials with 4 blocks of training conducted per day (total of ~400 trials per day). Target versus foil trials were pseudo-randomly ordered, each of which consisted of scan onset (imaging), pre-stimulus period (1.25 s), stimulus period (500 ms), delay (250 ms), a response period (1.75 s), and an inter-trial interval (ITI) with variable duration as described below. Mice only received water for correct responses to the target during the response period. Incorrect licks recorded after the foil presentation (a false alarm) were mildly punished by increasing the ITI. Animals were not punished if they licked during any other time epoch (i.e., if animal licked in the pre-stimulus period, tone presentation or delay period, the trial continued). This enabled us to confirm that animals were actively increasing lick rate for target tones during hit trials and reducing lick rate for foil tones during correct rejects (from baseline lick rate to zero during response window). This measurement confirmed that both the target and foil tone had behavioral effects on the animal; without this, animals could take a single-tone strategy (i.e., learn to lick only for the target tone or withhold licking for the foil tone).

Hit trial ITIs were 4–5 s (to enable full licking of reward), miss trials were not punished and had an ITI of 2–3 s, false alarm trials were punished with an ITI lasting 7–9 s, and correct rejects immediately moved to the next trial with an ITI of 2–3 s. Passive context was initiated immediately after completion of active context trial blocks. For layer 2/3 imaging experiments in **Figure 2**, a chamber light cue was briefly turned on, the lick tube was rotated out of place, and the light turned back off. Care was taken to not physically alter the position of the animal. For cell-type-specific imaging including excitatory neurons, interneuron imaging (**Fig. 3**) and axonal imaging of *ChAT-Cre* animals (**Fig. 5**), lick tube removal was automated using a micromanipulator and images were acquired for the entire duration of the experiment. For physiology experiments (**Figs. 4**–**6** and **Supplementary Fig. 11**), lick tube removal was performed within 5–10 s either manually or with an automated actuator and licks were detected with an infrared beam. In a subset of mice, licking was monitored using an infrared camera or beam to determine whether presentation of sound stimuli elicited a licking movement from the animal. Only in rare cases did mice lick for the target tone in the absence of the lick tube, and if they did, this behavior only lasted for 1–2 trials. In a subset of animals (n = 2), we established that the animals were still thirsty immediately after the passive trial, i.e., the animals would lick for *ad libitum* access to water, confirming that any changes in neuronal responses were not due to "satiety."

For muscimol experiments, animals were injected bilaterally with either saline vehicle or muscimol (1 μL of 1 mg/mL) at a depth of ~600 μm below the pial surface. The drug was allowed to diffuse while the animals were head-fixed for 10–15 min before behavior was initiated. In all cases, animals were tested with either saline injection or no injection the day after muscimol injections to determine if behavior recovered.

Behavior for physiology experiments. For physiology experiments, animals were trained on target and foil that were pre-selected before any physiological recordings (target = 9.5 kHz, foil = 5.6 kHz, 0.75 octave spacing). Given the typically shorter durations of whole-cell recordings, passive presentation was restricted to the target and foil, and lick tube removal (from active-to-passive) or insertion (passive-to-active) was performed in 5–7 s using either a manual manipulator or automated linear actuator. On the day immediately preceding whole-cell recordings, animals performed with $d' > 1.5$. Tone duration was set to 100 ms for training and experimentation. During training, hit ITIs were 4–5 s (to enable full licking of reward), miss trials were not punished and had an ITI of 2–3 s, false alarm trials were punished with an ITI lasting 7–9 s, and correct rejects immediately moved to the next trial with an ITI of 2–3 s. After animals were trained, false alarms were no longer punished during whole-cell recordings in order to maximize the number of trials while recordings were stable.

***In vivo* calcium imaging.** Two-photon fluorescence of GCaMP6s was excited at 900 nm using a mode locked Ti:Sapphire laser (MaiTai, Spectra-Physics, Mountain View, CA) and detected in the green channel (GFP emission). Imaging was performed on a multiphoton imaging system (Moveable Objective Microscope, Sutter Instruments) equipped with a water immersion objective (20×, NA = 0.95, Olympus) and the emission path was shielded from external light contamination. Images were collected using ScanImage (HHMI). To image auditory cortex, the objective was tilted to an angle of 50–60°. To record time courses of auditory-evoked neuronal activity, awake animals were head-fixed under the microscope and a speaker was placed adjacent to the microscope (microphone-ear distance ~10 cm). During auditory stimulation, ~300 μm^2 areas in layer 2/3 of A1 containing multiple GCaMP6s expressing neurons were selected and imaged (scan rate ~4 Hz, 0.26 s/frame, laser power ≤40 mW). For passive context, pure tones (70 dB SPL, 4–64 kHz, 500 ms, 10 ms cosine on/off ramps, quarter-octave spacing) were delivered in pseudo-random sequence every 20 frames (~5 s per passive context trial).

Motion correction. We used a multi-step approach to compensate for x–y motion due to movements of the awake mouse. First, we performed a frame-by-frame, rigid registration of the imaging frames that accounts for x–y changes in displacement, rotation and translation. Similar to published reports, a mean luminance-stable epoch from the middle of the session was chosen as the

© 2017 Nature America, Inc., part of Springer Nature. All rights reserved.

doi:10.1038/nn.4436

reference frame[51]. Second, in animals with a structural marker (tdTomato in PV$^+$ and VIP$^+$ interneurons) we separated the functional channel (green, GCaMP6s) from the structural channel (red, tdTomato). We then computed the tone-evoked response for fluorescent signal from both the functional green channel (GCaMPs) and the structural red channel (tdTomato). The red channel (tdTomato) had a small amount of fluorescence bleedthrough from the green fluorophore (GCaMP6s) that we could spectrally resolve using linear unmixing. We excluded data when the red channel exhibited stimulus-evoked "transients" that could not be explained by fluorescence bleedthrough (**Supplementary Fig. 6**). Third, in animals without a structural marker, we assessed the probability of motion-induced artifacts particularly at the moment of lick onset[52] by comparing the frequency of negative deflections with those of positive deflections during period of intense licking (**Supplementary Fig. 2**). Negative deflections in the fluorescent traces were immediately flagged and investigated as potentially due to motion out of the *z*-plane and were assumed to be highly correlated with false positives for positive deflections[35]. To remain conservative in our data inclusion criteria, any imaging planes that exhibited greater than 5% of cells with statistically-defined negative deflections (pairwise *t*-test of baseline versus negative peak) was excluded from the analysis ($n = 2$ planes out of 14 imaging planes). Fourth, for axonal imaging we focused our analysis entirely on tonic activity levels. After motion correction in the *x*–*y* plane, we identified epochs of time (10–20 s, 40–80 frames) where the amount of motion-correction in the active context (abs(d*x*) + abs(d*y*)) was similar to that in the passive context and less than 1.5 μm in either the *x*- or *y*-direction. This significantly reduced the probability that motion was contaminating the baseline activity levels of the measured axon segments. Fifth, to compare responses between contexts, we used a strict rule that the outline or shape of the cell, or axonal structure must be present in both contexts. We used the average intensity projection, the maximum intensity projection, and the motion-corrected time series to confirm this. Cells, in some instances, did not show up in both contexts (**Supplementary Fig. 3**) and were excluded from active-passive comparisons.

At all stages of the motion correction process, manual inspection was performed to identify motion out of the plane that was not able to be corrected by the above approach. In these rare cases, the data were excluded from further analysis.

Image processing and data analysis. Semi-automated data analysis was performed using custom-written software in ImageJ (NIH) and Matlab (MathWorks). Images were aligned as described above, cellular regions of interest (ROI) were manually drawn, and raw time-courses were extracted. For each cellular ROI and each behavioral condition, the response during tone stimulation was compared to background and "responsive" cells were identified statistically. We classified neurons as responsive if they showed a significant difference in their fluorescence signal immediately after tone presentation versus baseline ($P < 0.05$, Wilcoxon signed-rank test). Only responsive cells were used for further analysis. Deconvolution of calcium signals was performed and used for all comparisons across cells[53]. Results of behavior were analyzed in custom-written MATLAB programs with behavioral performance quantified in terms of fraction of correct trials, behavioral *d'*, and hit rate. For calcium imaging experiments, modulation index was calculated from the deconvolved calcium signals as [ΔSpike(active) – ΔSpike(passive)/ ΔSpike(active) + ΔSpike(passive)] similar to published reports using spiking data[2].

***In vitro* electrophysiology.** Acute slices of auditory cortex were prepared from adult mice (PV-tdTomato, SOM-tdTomato, and VIP-tdTomato). Animals were deeply anesthetized with a 1:1 ketamine/xylazine cocktail, perfused with dissection buffer and decapitated. The brain was rapidly placed in ice-cold dissection buffer containing (in mM): 87 NaCl, 75 sucrose, 2 KCl, 1.25 NaH_2PO_4, 0.5 $CaCl_2$, 7 $MgCl_2$, 25 $NaHCO_3$, 1.3 ascorbic acid, and 10 dextrose, bubbled with 95%/5% O2/CO2 (pH 7.4). Slices (300–400 μm thick) were prepared with a vibratome (Leica), placed in warm dissection buffer (33–35 °C) for <30 min, then transferred to a holding chamber containing warmed artificial cerebrospinal fluid (ACSF) (in mM: 124 NaCl, 2.5 KCl, 1.5 $MgSO_4$, 1.25 NaH_2PO_4, 2.5 $CaCl_2$, and 26 $NaHCO_3$). Slices were kept at room temperature (22–24 °C) for >25 min before use. For experiments, slices were transferred to the recording chamber and perfused (2–2.5 ml min−1) with oxygenated ACSF at 33 °C.

Somatic whole-cell recordings were made from layer 2/3 pyramidal cells. Recordings were performed in current-clamp mode with a Multiclamp 700B amplifier (Molecular Devices) using IR-DIC video microscopy (Olympus). Patch pipettes (5–8 MΩ) were filled with intracellular solution (in mM: 135 K-gluconate, 5 NaCl, 10 HEPES, 5 MgATP, 10 phosphocreatine, and 0.3 GTP). For blocking synaptic activity, we used DNQX (10 mM), APV (25 mM), picrotoxin (10 mM), and muscarine (1–2 μM). The mean series resistance (R_s) was 27.4 ± 10.4 MΩ (s.d., s.d.) and the mean input resistance (R_i) was 88.7 ± 25.8 MΩ, determined by monitoring cells with hyperpolarizing pulses (40 pA for 50 ms). Recordings were excluded from analysis if R_s or R_i changed >30% compared to the baseline period. Data were digitized at 10 kHz and analyzed with Clampfit 10 (Molecular Devices). Picrotoxin, DNQX, and APV were purchased from Sigma. All statistics and error bars are reported as means ± s.e.m. and statistical significance assessed with paired two-tailed Student's *t*-tests.

***In vivo* electrophysiology.** *In vivo* whole-cell recordings were performed in a sound-attenuating chamber, and recordings obtained from auditory cortical neurons with a Multiclamp 700B amplifier (Molecular Devices). For voltage-clamp recordings, pipettes contained: 130 Cs-methanesulfonate, 1 QX-314, 4 TEA-Cl, 0.5 BAPTA, 4 MgATP, 20 phosphocreatine, 10 HEPES, pH 7.2. Whole-cell recordings from A1 neurons were obtained from cells located within 400 μm of the pial surface, in putative layer 2/3. Data were filtered at 5 kHz, digitized at 20 kHz, and analyzed with Clampfit 10 (Molecular Devices). R_s: 47.4 ± 31.6 MΩ; R_i: 154 ± 150 MΩ (s.d.) in 38 cells. Recordings were excluded from analysis if R_s or R_i changed >30% relative to the either passive or active context. For all included cells, we also examined the correlation between changes to synaptic currents and changes to R_i and R_s for both IPSCs and EPSCs and observed no correlation (ΔIPSC: $r = -0.13$, $P = 0.62$ for R_s, $r = -0.17$, $P = 0.51$ for R_i; ΔEPSC: $r = -0.06$, $P = 0.82$ for R_s, $r = -0.05$, $P = 0.85$ for R_i). We used a preparation which enabled access to auditory cortex via a ~200 μm hole in a 3 mm piece of round glass, providing the stability required to hold cells across conditions[54] (**Fig. 4a**).

Pure tones (100 ms duration, 3 ms cosine on/off ramps) for target and foil (5–10 kHz) were played at 70 dB SPL. Tone-evoked responses were measured in a tone onset and offset window (150 ms) starting at tone onset. Power analysis was performed to determine sample size for statistical significance with a power of β:0.7; these studies required at least three neurons for differences in synaptic currents during regular behavior between contexts, five neurons for pharmacology experiments, and three neurons for optogenetics experiments, all satisfied in the experiments of **Figures 4** and **6** and **Supplementary Figure 11**. For all patch-clamp experiments, IPSCs and EPSCs values were calculated using the peak amplitude during the tone (for tone onset neurons) or during and immediately after the tone (for tone offset neurons). The modulation index was calculated relative to the active context (Active – Passive)/Active.

For atropine experiments, 1 mM atropine was topically applied through a hole in the cranial window for at least 30 min before patch-clamp experiments or behavior; control experiments were performed with saline. For cholinergic modulation via optogenetic stimulation in *ChAT-ChR2-EYFP* mice, blue light was delivered to the brain surface via a 200 μm fiber (Thorlabs) positioned ~0.5 mm above the brain surface, coupled to a 473 nm laser (CrystaLaser). During whole-cell recordings, blue light pulses were triggered 100 ms before tone onset and lasted for 375 ms (473 nm wavelength, 2–2.5 mW) at the surface of the brain. During desynchronization experiments (**Supplementary Fig. 12**), 473 nm light was delivered in a 5 s square pulse at 5 mW mm^{-2}. LFP recordings were made using a 0.5 MΩ tungsten electrode, and were acquired at 20 kHz. For spectral analysis in **Supplementary Figure 12**, we down-sampled LFP recordings to 200 Hz, then performed time-frequency decomposition of the LFP using custom software written in Matlab. We used a 1 s sliding window with 50 ms steps and averaged spectra across trials. The spectra shown in **Supplementary Figure 12** were obtained from 10 trials of 5 s square laser pulses delivered to auditory cortex. Each frequency band was normalized by the average power in the 2 s baseline period preceding cortical optical stimulation. Changes in synaptic responses in **Figures 4** and **5** and **Supplementary Figures 8** and **11** were compared by Student's paired two-tailed *t*-tests as data passed Kolmogorov-Smirnov normality tests.

For interneuron inactivation experiments, AAV1.EF1a.DIO.eNpHR3.0 was injected unilaterally into the auditory cortex of *PV-cre, SOM-cre, or VIP-cre* mice at least 2 weeks before any electrophysiological or optogenetic experiments. On the first day of recording, we removed the skull only above auditory cortex and implanted a cranial window for optical illumination with a small access hole for the patch electrode. We then restricted optical illumination to auditory cortex

© 2017 Nature America, Inc., part of Springer Nature. All rights reserved.

with a fiber-coupled laser. During whole-cell recordings or behavioral sessions, blue light pulses were triggered 100 ms before tone onset and lasted for 300 ms (532nm wavelength, 10–20 mW/mm^2) at the surface of the brain.

Integrate-and-fire model of synaptic currents. The simulations in **Supplementary Figure 7** used a conductance-based integrate-and-fire model neuron similar to our previous study relating synaptic currents and spike generation[28]. For simulating the spiking patterns of each cell, we used EPSCs and IPSCs from experiments in **Figure 4**. On each trial, one EPSC and one IPSC were randomly chosen from the set of recorded responses. Excitatory and inhibitory synaptic conductances (g_e and g_i, respectively) were computed from currents as previously described[28], and then g_e and g_i were randomly rescaled on each trial to have peak instantaneous conductance over the range 1.0–1.7 nS. Membrane voltage was computed as:

$$\tau_m \frac{(dV)}{dt} = V_{\text{rest}} - V + g_e(t)\left(E_e - V\right) + g_i(t)\left(E_i - V\right),$$

with τ_m = 10 ms, resting membrane potential V_{rest} = −70 mV, excitatory reversal potential E_e = 0 mV, and inhibitory reversal potential E_i = −70 mV. A spike was evoked in the postsynaptic neuron if the membrane voltage reached threshold of −40 mV, at which point the membrane potential was reset to −80 mV in the next time step. Spike rates and trial-by-trial correlation were determined over 100–200 trials (to ensure sampling from the full set of EPSCs and IPSCs), and full rasters for all modeled trials are displayed in **Supplementary Figure 7c** for each simulation. Code can be obtained at: http://froemkelab.med.nyu.edu/kuchibhotla_etal_simulations.

Network model: 4-unit model. We built a circuit model of auditory cortex containing four populations: one excitatory and one for each of the three inhibitory subtypes (PV, VIP, and SOM). Each population is represented by a single rate-based equation:

$$\tau_x \frac{dr_x}{dt} = -r_x + f(I_x^{tot})$$

with

$$I_x^{tot} = \sum_y W_{xy} r_y + I_x^B + I_x^T + I_x^A$$

where r_x is the firing rate of the X cell population (with X = E, P, V, S). The time constants were the same for all I subtypes ($\tau_{P,V,S}$ = 10 ms) and slower for the E population (τ_E = 20 ms). f is the neural activation function. Here we use a rectified power law[55]:

$$f\left(I_x^{tot}\right) = k\left(\left[I_x^{tot}\right]_+\right)^n$$

with k = 0.01 and n = 2.2. Use of a rectified linear activation function (k = 1, n = 1) provided qualitatively similar results.

Connections between populations are given via a weight matrix:

$$W = \begin{bmatrix} W_{EE} & W_{EP} & W_{EV} & W_{ES} \\ W_{PE} & W_{PP} & W_{PV} & W_{PS} \\ W_{VE} & W_{VP} & W_{VV} & W_{VS} \\ W_{SE} & W_{SP} & W_{SV} & W_{SS} \end{bmatrix}$$

Values for inhibitory connections were determined using data from visual cortex[56], with the addition of a VIP-to-PV connection known to exist in auditory cortex[31] (note that the results do not depend on this connection). Values for excitatory connections were determined from empirical and modeling studies[57,58], and all weights were fit to ensure they produced reasonable firing rates. This produced the following set of values:

$$W = \begin{bmatrix} .017 & -.956 & -.045 & -.512 \\ .8535 & -.99 & -.09 & -.307 \\ 2.104 & -.184 & 0 & -.734 \\ 1.285 & 0 & -.14 & 0 \end{bmatrix}$$

Constant background input is given to all four populations in order to create reasonable spontaneous rates (IEB = 12.8, IPB = 24, IVB = 8, ISB = 9.6). Tone-related input is given only to the excitatory and PV populations, for the duration of the tone (IET = 93, IPT = 74, 100 ms)[59]. The strength of the tone-related inputs were chosen such that they elicited tone-evoked firing rates in each of the four populations that were consistent with reported rates in auditory cortex[60,61].

For modeling of the passive condition, no ACh inputs are given (IA = 0). In the active condition, the effects of ACh are modeled as a small additional input to all three inhibitory populations (unless otherwise noted), based on the reported depolarizing effects of ACh on these cell types (IpA = IVA = ISA = 5, though the results are robust to differences in IA across subtypes (**Supplementary Fig. 13**). Spontaneous and evoked rates in both conditions were determined using steady state values of the model. However, measuring tone-evoked rates using either peak values or rates averaged over the initial tone-evoked transients (50 ms) produced qualitatively similar results.

To test for robustness, the following parameters of the model were varied independently from −10% to +10% of their current values: IET, IPT, IpA, IVA, ISA, and all nonzero entries of W. Out of 5,000 simulations run with these randomly chosen parameters, all but one produced correct directional changes due to ACh in all four cell types. Thus, the model is robust to parameter variations in this range. All simulations were run using the forward Euler method with 0.5-ms time step.

Network model: multi-unit. In order to explore diversity within a cell type population, the four unit model described above was expanded into a multi-unit model, wherein each cell subtype was represented by multiple individual rate-based units rather than just one. The number of cells per population varied by subtype (NE = 800, NP = 100, NV = 50, NS = 50). Assuming the following connection probabilities between subtypes (though results are comparable for a range of connection probabilities):

$$P = \begin{bmatrix} .15 & .3 & .3 & .3 \\ .3 & .3 & .3 & .3 \\ .3 & .3 & 0 & .3 \\ .3 & 0 & .3 & 0 \end{bmatrix}$$

The mean synaptic strength between different cell types was calculated by dividing the weight between the cell types by the product of the connection probability and the number of cells in the presynaptic population: GXY = WXY/(NY*PXY). This gives:

$$G = \begin{bmatrix} .0001 & -.0319 & -.0030 & -.0341 \\ .0036 & -.0330 & -.0060 & -.0205 \\ .0083 & -.0061 & 0 & -.0489 \\ .0054 & 0 & -.0093 & 0 \end{bmatrix}$$

Actual synaptic strengths were drawn from a lognormal distribution with the given mean and variance equaling one-ninth the mean. (Note: the mean E to VIP connection was lowered slightly as compared to the 4-unit model, as it provided a better fit to the desired firing rates in the multi-unit model).

Similar to the 4-unit model, background input was given to all cells to maintain reasonable spontaneous rates with values as in the 4-unit model. Tone inputs were given to all E and PV cells only; tone-related inputs were drawn independently for each cell on each trial from a Gaussian with mean values as in the 4-unit model and a variance of 2. ACh inputs were given to all PV, VIP, and SOM cells but drawn independently for each cell, and held constant across trials, from a Gaussian with a mean value of 5 and variance of 10 (truncated so that all values remain positive). This variance of cholinergic effects was intended to represent the likely variability in the nature of cholinergic innervation in auditory cortex.

Results were calculated using 20 realizations of the network, run with 15 trials each for passive and active conditions. The multi-unit model matches the 4-unit model in terms of average spontaneous and evoked firing rates, and average changes in firing rate due to ACh.

Histology. To confirm the specific expression of the genetically encoded calcium indicator GCaMP6s in nucleus basalis cholinergic neurons following injection in ChAT-Cre mice, we performed ChAT immunohistochemistry. We performed similar histology with different antibodies to confirm eNpHR3.0 expression in

© 2017 Nature America, Inc., part of Springer Nature. All rights reserved.

doi:10.1038/nn.4436

interneuron Cre lines and selective expression of CAMK2-GCaMP6f in excitatory neurons preferentially (**Supplementary Fig. 14**). Mice were transcardially perfused using ~45 mL PBS followed by ~45 mL 4% PFA under deep anesthesia. Brains were extracted from the skull and post-fixed in 4% PFA for ~2 h at 4 °C, then cryoprotected overnight in 30% sucrose solution and sliced coronally with 16 µm thickness on a cryostat. Fixed brain sections were washed with PBS, then incubated for 2–3 h at room temperature in blocking buffer containing PBS with 0.5% v/v Triton X-100 (Sigma), 2% v/v normal goat serum (Life Technologies) and 50 mg/mL BSA. The blocking solution was aspirated and the slices were incubated in primary antibody (1:1,000 dilution of chicken anti-GFP IgY, cat. # ab13970 (Abcam); 1:200 rabbit anti-ChAT IgG, cat. # AB143 (Millipore); 1:1,000 dilution of VIP antibody IgG, product. #20077 (Immunostar); 1:1,000 dilution of anti-parvalbumin IgG, code #235 (Swant); 1:500 dilution of anti-somatostatin IgG, clone YC7, cat. # MAB354 (Millipore)) overnight at 4 °C. Afterwards, slices were washed and incubated for 1–2 h at room temperature in secondary antibody (1:1,000 dilution, goat anti-chicken IgY Alexa Fluor 488, cat. # A11039; goat anti-rabbit IgG Alexa Fluor 555, cat. # A21430, both from Life Technologies; 1:1,000 dilution of goat anti-mouse IgG Alexa Fluor 555, cat. # A21422 (Life Technologies); 1:500 dilution of goat anti-rat IgG, Alexa Fluor 555, cat. # A21434 (Life Technologies)). Finally, slides were washed, incubated at room temperature in DAPI/Hoechst solution (1:1,000 in PBS), washed, then coverslipped using Fluoromount (Sigma). Images were acquired from nucleus basalis with a 20× air objective on a Zeiss LSM 710 Confocal Microscope (Carl Zeiss Inc.) and cell counts were performed in Image J (NIH). All cells stained with both anti-ChAT and anti-GFP antibodies were considered cholinergic and expressing GCaMP6s. Overall, 95.2 ± 2.6% ($n = 3$ mice) of GCaMP6s$^+$ cells were ChAT$^+$ ($n = 3$ mice, 15 images), and 50% of ChAT$^+$ cells were GCaMP6s$^+$ ($n = 3$ mice, 15 images). All cells counted had confirmed nuclear DAPI staining.

Statistical analysis. All statistical analyses were performed in MATLAB or GraphPad Prism 6. Data sets were tested for normality, and appropriate statistical tests applied as described in the text (for example, *t*-test for normally distributed data, Fischer's exact test for categorical observations, Mann Whitney *U*-test for non-parametric data, Friedman test with Dunn *post hoc* test for non-parametric data with repeated measurements). Shaded regions surrounding line-plots indicate ± s.e.m. unless otherwise stated. Unless indicated in the methods, no statistical methods were used to pre-determine sample sizes, but our sample sizes are similar to those reported in previous publications[7,8,48,51]. Data collection and analysis were not performed blind to the conditions of the experiments.

Data availability statement. The data that support the findings of this study are available from the corresponding author upon reasonable request. All code related to the modeling work is available at http://froemkelab.med.nyu.edu/.

A **Supplementary Methods Checklist** is available.

51. Huber, D. *et al.* Multiple dynamic representations in the motor cortex during sensorimotor learning. *Nature* **484**, 473–478 (2012).
52. Chen, J.L., Pfäffli, O.A., Voigt, F.F., Margolis, D.J. & Helmchen, F. Online correction of licking-induced brain motion during two-photon imaging with a tunable lens. *J. Physiol. (Lond.)* **591**, 4689–4698 (2013).
53. Vogelstein, J.T. *et al.* Fast nonnegative deconvolution for spike train inference from population calcium imaging. *J. Neurophysiol.* **104**, 3691–3704 (2010).
54. Vallentin, D., Kosche, G., Lipkind, D. & Long, M.A. Neural circuits. Inhibition protects acquired song segments during vocal learning in zebra finches. *Science* **351**, 267–271 (2016).
55. Miller, K.D. & Troyer, T.W. Neural noise can explain expansive, power-law nonlinearities in neural response functions. *J. Neurophysiol.* **87**, 653–659 (2002).
56. Pfeffer, C.K., Xue, M., He, M., Huang, Z.J. & Scanziani, M. Inhibition of inhibition in visual cortex: the logic of connections between molecularly distinct interneurons. *Nat. Neurosci.* **16**, 1068–1076 (2013).
57. Hofer, S.B. *et al.* Differential connectivity and response dynamics of excitatory and inhibitory neurons in visual cortex. *Nat. Neurosci.* **14**, 1045–1052 (2011).
58. Litwin-Kumar, A., Rosenbaum, R. & Doiron, B. Inhibitory stabilization and visual coding in cortical circuits with multiple interneuron subtypes. *J. Neurophysiol.* **115**, 1399–1409 (2016).
59. Ji, X.Y. *et al.* Thalamocortical innervation pattern in mouse auditory and visual cortex: laminar and cell-type specificity. *Cereb. Cortex* **26**, 2612–2625 (2016).
60. Chen, I.W., Helmchen, F. & Lutcke, H. Specific early and late oddball-evoked responses in excitatory and inhibitory neurons of mouse auditory cortex. *J. Neurosci.* **35**, 12560–12573 (2015).
61. Mesik, L. *et al.* Functional response properties of VIP-expressing inhibitory neurons in mouse visual and auditory cortex. *Front. Neural Circuits* **9**, 22 (2015).

© 2017 Nature America, Inc., part of Springer Nature. All rights reserved.